

1

<sup>2</sup>A SEARCH FOR LONG-LIVED, CHARGED, SUPERSYMMETRIC PARTICLES  
<sup>3</sup>USING IONIZATION WITH THE ATLAS DETECTOR

4

BRADLEY AXEN

5

September 2016 – Version 0.33

6



<sup>8</sup> Bradley Axen: *A Search for Long-Lived, Charged, Supersymmetric Particles using*  
<sup>9</sup> *Ionization with the ATLAS Detector*, Subtitle, © September 2016

10

Usually a quotation.

11

Dedicated to.



<sub>12</sub> ABSTRACT

---

<sub>13</sub> How to write a good abstract:

<sub>14</sub> <https://plg.uwaterloo.ca/~migod/research/beck00PSLA.html>



<sub>15</sub> PUBLICATIONS

---

<sub>16</sub> Some ideas and figures have appeared previously in the following publications:

<sub>17</sub>

<sub>18</sub> Put your publications from the thesis here. The packages `multibib` or `bibtopic`  
<sub>19</sub> etc. can be used to handle multiple different bibliographies in your document.



---

<sup>21</sup> ACKNOWLEDGEMENTS

<sup>22</sup> Put your acknowledgements here.

<sup>23</sup>

<sup>24</sup> And potentially a second round.

<sup>25</sup>



26 CONTENTS

---

27	I	INTRODUCTION	1
28	1	INTRODUCTION	3
29	II	THEORETICAL CONTEXT	5
30	2	STANDARD MODEL	7
31	2.1	Particles . . . . .	7
32	2.2	Interactions . . . . .	8
33	2.3	Limitations . . . . .	8
34	3	SUPERSYMMETRY	9
35	3.1	Motivation . . . . .	9
36	3.2	Structure . . . . .	9
37	3.3	Phenomenology . . . . .	9
38	4	LONG-LIVED PARTICLES	11
39	4.1	Mechanisms . . . . .	11
40	4.1.1	Examples in Supersymmetry . . . . .	11
41	4.2	Phenomenology . . . . .	11
42	4.2.1	Disimilarities to Prompt Decays . . . . .	11
43	4.2.2	Characteristic Signatures . . . . .	11
44	III	EXPERIMENTAL STRUCTURE AND RECONSTRUCTION	13
45	5	THE LARGE HADRON COLLIDER	15
46	5.1	Injection Chain . . . . .	15
47	5.2	Design and Parameters . . . . .	15
48	5.3	Luminosity . . . . .	15
49	6	THE ATLAS DETECTOR	17
50	6.1	Coordinate System . . . . .	17
51	6.2	Magnetic Field . . . . .	17
52	6.3	Inner Detector . . . . .	17
53	6.3.1	Pixel Detector . . . . .	17
54	6.3.2	Semiconductor Tracker . . . . .	17
55	6.3.3	Transition Radiation Tracker . . . . .	17
56	6.4	Calorimetry . . . . .	17
57	6.4.1	Electromagnetic Calorimeters . . . . .	17
58	6.4.2	Hadronic Calorimeters . . . . .	17
59	6.4.3	Forward Calorimeters . . . . .	17
60	6.5	Muon Spectrometer . . . . .	17
61	6.6	Trigger . . . . .	17
62	6.6.1	Trigger Scheme . . . . .	17
63	6.6.2	Missing Transverse Energy Triggers . . . . .	17
64	7	EVENT RECONSTRUCTION	19
65	7.1	Tracks and Vertices . . . . .	19

66	7.1.1	Track Reconstruction . . . . .	19
67	7.1.2	Vertex Reconstruction . . . . .	19
68	7.2	Jets . . . . .	19
69	7.2.1	Topological Clustering . . . . .	19
70	7.2.2	Jet Energy Scale . . . . .	19
71	7.2.3	Jet Energy Scale Uncertainties . . . . .	19
72	7.2.4	Jet Energy Resolution . . . . .	19
73	7.3	Electrons . . . . .	19
74	7.3.1	Electron Identification . . . . .	19
75	7.4	Muons . . . . .	19
76	7.4.1	Muon Identification . . . . .	19
77	7.5	Missing Transverse Energy . . . . .	19
78	IV	CALORIMETER RESPONSE	21
79	8	RESPONSE MEASUREMENT WITH SINGLE HADRONS	23
80	8.1	Dataset and Simulation . . . . .	24
81	8.1.1	Data Samples . . . . .	24
82	8.1.2	Simulated Samples . . . . .	24
83	8.1.3	Event Selection . . . . .	24
84	8.2	Inclusive Hadron Response . . . . .	25
85	8.2.1	E/p Distribution . . . . .	25
86	8.2.2	Zero Fraction . . . . .	26
87	8.2.3	Neutral Background Subtraction . . . . .	27
88	8.2.4	Corrected Response . . . . .	29
89	8.2.5	Additional Studies . . . . .	31
90	8.3	Identified Particle Response . . . . .	34
91	8.3.1	Decay Reconstruction . . . . .	34
92	8.3.2	Identified Response . . . . .	35
93	8.3.3	Additional Species in Simulation . . . . .	37
94	8.4	Summary . . . . .	38
95	9	JET ENERGY RESPONSE AND UNCERTAINTY	41
96	9.1	Motivation . . . . .	41
97	9.2	Uncertainty Estimate . . . . .	41
98	9.3	Summary . . . . .	44
99	V	SEARCH FOR LONG-LIVED PARTICLES	47
100	10	LONG-LIVED PARTICLES IN ATLAS	49
101	10.1	Event Topology . . . . .	49
102	10.1.1	Detector Interactions . . . . .	50
103	10.1.2	Lifetime Dependence . . . . .	50
104	10.2	Simulation . . . . .	52
105	11	EVENT SELECTION	53
106	11.1	Trigger . . . . .	54
107	11.2	Kinematics and Isolation . . . . .	54
108	11.3	Standard Model Rejection . . . . .	57
109	11.4	Ionization . . . . .	60
110	11.4.1	Mass Estimation . . . . .	60

111	11.5 Efficiency . . . . .	61
112	12 BACKGROUND ESTIMATION	65
113	12.1 Background Sources . . . . .	65
114	12.2 Prediction Method . . . . .	66
115	12.3 Validation . . . . .	67
116	12.3.1 Closure in Simulation . . . . .	67
117	12.3.2 Validation Region in Data . . . . .	68
118	13 SYSTEMATIC UNCERTAINTIES AND RESULTS	71
119	13.1 Systematic Uncertainties . . . . .	71
120	13.2 Final Yields . . . . .	71
121	14 INTERPRETATION	73
122	14.1 Cross Sectional Limits . . . . .	73
123	14.2 Mass Limits . . . . .	73
124	14.3 Context for Long-Lived Searches . . . . .	73
125	<b>VI CONCLUSIONS</b>	75
126	15 SUMMARY AND OUTLOOK	77
127	15.1 Summary . . . . .	77
128	15.2 Outlook . . . . .	77
129	<b>VII APPENDIX</b>	79
130	A INELASTIC CROSS SECTION	81
131	B APPENDIX TEST	83
132	B.1 Appendix Section Test . . . . .	83
133	B.1.1 Appendix Subection Test . . . . .	83
134	B.2 A Table and Listing . . . . .	83
135	B.3 Some Formulas . . . . .	84
136	<b>BIBLIOGRAPHY</b>	87

137 LIST OF FIGURES

---

138	Figure 1	The particle content of the Standard Model (SM). . . . .	8
139	Figure 2	An illustration (a) of the $E/p$ variable used throughout this paper. The red energy deposits come from the charged particle targeted for measurement, while the blue energy deposits are from nearby neutral particles and must be subtracted. The same diagram (b) for the neutral-background selection, described in Section 8.2.3.	26
140			
141			
142			
143			
144			
145	Figure 3	The $E/p$ distribution and ratio of simulation to data for isolated tracks with (a) $ \eta  < 0.6$ and $1.2 < p/\text{GeV} < 1.8$ and (b) $ \eta  < 0.6$ and $2.2 < p/\text{GeV} < 2.8$ . . . . .	26
146			
147			
148	Figure 4	The fraction of tracks as a function (a, b) of momentum, (c, d) of interaction lengths with $E \leq 0$ for tracks with positive (on the left) and negative (on the right) charge. . . . .	28
149			
150			
151			
152	Figure 5	$\langle E/p \rangle_{\text{BG}}$ as a function of the track momentum for tracks with (a) $ \eta  < 0.6$ , (b) $0.6 <  \eta  < 1.1$ , and as a function of the track pseudorapidity for tracks with (c) $1.2 < p/\text{GeV} < 1.8$ , (d) $1.8 < p/\text{GeV} < 2.2$ . . . . .	29
153			
154			
155			
156	Figure 6	$\langle E/p \rangle_{\text{COR}}$ as a function of track momentum, for tracks with (a) $ \eta  < 0.6$ , (b) $0.6 <  \eta  < 1.1$ , (c) $1.8 <  \eta  < 1.9$ , and (d) $1.9 <  \eta  < 2.3$ . . . . .	30
157			
158			
159	Figure 7	$\langle E/p \rangle_{\text{COR}}$ calculated using LCW-calibrated topological clusters as a function of track momentum for tracks with (a) zero or more associated topological clusters or (b) one or more associated topological clusters. . . . .	31
160			
161			
162			
163	Figure 8	Comparison of the $\langle E/p \rangle_{\text{COR}}$ for tracks with (a) less than and (b) greater than 20 hits in the TRT. . . . .	32
164			
165	Figure 9	Comparison of the $\langle E/p \rangle_{\text{COR}}$ for (a) positive and (b) negative tracks as a function of track momentum for tracks with $ \eta  < 0.6$ . . . . .	32
166			
167			
168	Figure 10	Comparison of the $E/p$ distributions for (a) positive and (b) negative tracks with $0.8 < p/\text{GeV} < 1.2$ and $ \eta  < 0.6$ , in simulation with the FTFP_BERT and QGSP_BERT physics lists. . . . .	33
169			
170			
171			
172	Figure 11	Comparison of the response of the hadronic calorimeter as a function of track momentum (a) at the EM-scale and (b) after the LCW calibration. . . . .	33
173			
174			
175	Figure 12	Comparison of the response of the EM calorimeter as a function of track momentum (a) at the EM-scale and (b) with the LCW calibration. . . . .	34
176			
177			

178	Figure 13	The reconstructed mass peaks of (a) $K_S^0$ , (b) $\Lambda$ , and (c) $\bar{\Lambda}$ candidates. . . . .	35
179			
180	Figure 14	The $E/p$ distribution for isolated (a) $\pi^+$ , (b) $\pi^-$ , (c) proton, and (d) anti-proton tracks. . . . .	36
181			
182	Figure 15	The fraction of tracks with $E \leq 0$ for identified (a) $\pi^+$ and $\pi^-$ , and (b) proton and anti-proton tracks . . . . .	36
183			
184	Figure 16	The difference in $\langle E/p \rangle$ between (a) $\pi^+$ and $\pi^-$ (b) $p$ and $\pi^+$ , and (c) $\bar{p}$ and $\pi^-$ . . . . .	37
185			
186	Figure 17	$\langle E/p \rangle_{\text{COR}}$ as a function of track momentum for (a) $\pi^+$ tracks and (b) $\pi^-$ tracks. . . . .	38
187			
188	Figure 18	The ratio of the calorimeter response to single parti- cles of various species to the calorimeter response to $\pi^+$ with the physics list FTFP_BERT. . . . .	38
189			
190	Figure 19	The spectra of true particles inside anti- $k_t$ , $R = 0.4$ jets with (a) $90 < p_T/\text{GeV} < 100$ , (b) $400 < p_T/\text{GeV} <$ $500$ , and (c) $1800 < p_T/\text{GeV} < 2300$ . . . . .	42
191			
192	Figure 20	The jet energy scale ( $\text{JES}$ ) uncertainty contributions, as well as the total $\text{JES}$ uncertainty, as a function of jet $p_T$ for (a) $ \eta  < 0.6$ and (b) $0.6 <  \eta  < 1.1$ . . . . .	44
193			
194	Figure 21	The $\text{JES}$ correlations as a function of jet $p_T$ and $ \eta $ for jets in the central region of the detector. . . . .	45
195			
196	Figure 22	The distribution of $E_T^{\text{miss}}$ for data and simulated signal events, after the trigger requirement. . . . .	55
197			
198	Figure 23	The dependence of $dE/dx$ on $N_{\text{split}}$ in data after basic track hit requirements have been applied. . . . .	56
199			
200	Figure 24	The distribution of $dE/dx$ with various selections ap- plied in data and simulated signal events. . . . .	57
201			
202	Figure 25	The distribution of track momentum for data and sim- ulated signal events, after previous selection require- ments have been applied. . . . .	58
203			
204	Figure 26	The distribution of $M_T$ for data and simulated sig- nal events, after previous selection requirements have been applied. . . . .	59
205			
206	Figure 27	The distribution of summed tracked momentum within a cone of $\Delta R < 0.25$ around the candidate track for data and simulated signal events, after previous selec- tion requirements have been applied. . . . .	60
207			
208	Figure 28	The normalized, two-dimensional distribution of $E/p$ and $f_{\text{EM}}$ for simulated (a) $Z \rightarrow ee$ , (b) $Z \rightarrow \tau\tau$ , (c) 1200 GeV Stable R-Hadron events, and (d) 1200 GeV, 10 ns R-Hadron events. . . . .	61
209			
210	Figure 29	Two-dimensional distribution of $dE/dx$ versus charge signed momentum ( $qp$ ) for minimum-bias tracks. The fitted distributions of the most probable values for pi- ons, kaons and protons are superimposed. . . . .	62
211			
212			
213			
214			
215			
216			
217			
218			
219			
220			
221			
222			

223	Figure 30	The distribution of mass estimated using $dE/dx$ for simulated stable R-Hadrons with masses between 1000 and 1600 GeV. . . . .	62
224			
225			
226	Figure 31	The acceptance $\times$ efficiency as a function of R-Hadron (a) mass and (b) lifetime. (a) shows all of the combinations of mass and lifetime considered in this search, and (b) highlights the lifetime dependence for 1000 GeV and 1600 GeV R-Hadrons. . . . .	64
227			
228			
229			
230			
231	Figure 32	The distribution of (a) $dE/dx$ and (b) momentum for tracks in data and simulated signal after requiring the event level selection and the track selection on $p_T$ , hits, and $N_{\text{split}}$ . Each sub-figure shows the normalized distributions for tracks classified as hadrons, electrons, and muons in data and R-Hadrons in the simulated signal. . . . .	66
232			
233			
234			
235			
236			
237			
238	Figure 33	The distribution of $M_{dE/dx}$ (a) before and (b) after the ionization requirement for tracks in simulated W boson decays and for the randomly generated background estimate. . . . .	68
239			
240			
241			
242	Figure 34	The distribution of $M_{dE/dx}$ (a) before and (b) after the ionization requirement for tracks in the validation region and for the randomly generated background estimate. . . . .	69
243			
244			
245			

246 LIST OF TABLES

258 LISTINGS

---

<small>259</small>	Listing 1	A floating example ( <code>listings</code> manual) . . . . .	84
--------------------	-----------	--	----

260 ACRONYMS

---

- 261 SM Standard Model  
262 SUSY Supersymmetry  
263 LSP Lightest Supersymmetric Particle  
264 LHC Large Hadron Collider  
265 ATLAS A Toroidal LHC ApparatuS  
266 ToT time over threshold  
267 LCW local cluster weighted  
268 MIP minimally ionizing particle  
269 EPJC European Physical Journal C  
270 JES jet energy scale  
271 LLP Long-Lived Particle  
272 CR Control Region



273

## PART I

274

### INTRODUCTION

275

You can put some informational part preamble text here.



# 1

276

277 INTRODUCTION

---



278

## PART II

279

### THEORETICAL CONTEXT

280

You can put some informational part preamble text here.



# 2

281

## 282 STANDARD MODEL

---

283 The SM of particle physics seeks to explain the symmetries and interactions of  
284 all currently discovered fundamental particles. It has been tested by several genera-  
285 tions of experiments and has been remarkably successful, no significant de-  
286 viations have been found. The SM provides predictions in particle physics for  
287 interactions up to the Planck scale ( $10^{15}$ - $10^{19}$  GeV).

288 The theory itself is a quantum field theory grown from an underlying  $SU(3) \times$   
289  $SU(2) \times U(1)$  that requires the particle content and quantum numbers consist-  
290 ent with experimental observations (see Section 2.1). Each postulated symme-  
291 try is accompanied by an interaction between particles through gauge invari-  
292 ance. These interactions are referred to as the Strong, Weak, and Electromag-  
293 netic forces, which are discussed in Section 2.2.

294 Although this model has been very predictive, the theory is incomplete; for  
295 example, it is not able to describe gravity or astronomically observed dark matter.  
296 These limitations are discussed in more detail in Section 2.3.

## 297 21 PARTICLES

298 The most familiar matter in the universe is made up of protons, neutrons, and  
299 electrons. Protons and neutrons are composite particles, however, and are made  
300 up in turn by particles called quarks. Quarks carry both electric charge and color  
301 charge, and are bound in color-neutral combinations called baryons. The elec-  
302 tron is an example of a lepton, and carries only electric charge. Another type  
303 of particle, the neutrino, does not form atomic structures in the same way that  
304 quarks and leptons do because it carries no color or electric charge. Collectively,  
305 these types of particles are known as fermions, the group of particles with half-  
306 integer spin.

307 There are three generations of fermions, although familiar matter is formed  
308 predominantly by the first generation. The generations are identical except for  
309 their masses, which increase in each generation by convention. In addition, each  
310 of these particles is accompanied by an antiparticle, with opposite-sign quantum  
311 numbers but the same mass.

312 The fermions comprise what is typically considered matter, but there are  
313 additional particles that are mediators of interactions between those fermions.  
314 These mediators are known as the gauge bosons, gauge in that their existence  
315 is required by gauge invariance (discussed further in Section 2.2) and bosons in  
316 that they have integer spin. The boson which mediates the electromagnetic force  
317 is the photon, the first boson to be discovered; it has no electric charge, no mass,  
318 and a spin of 1. There are three spin-1 mediators of the weak force, the two  
319 W bosons and the Z boson. The W bosons have electric charge of  $\pm 1$  and a  
320 mass of  $80.385 \pm 0.015$  GeV, while the Z boson is neutral and has a mass of

321 91.1876  $\pm$  0.0021 GeV. The strong force is mediated by eight particles called  
 322 gluons, which are massless and electrically neutral but do carry color charge.

323 The final particle present in the SM is the Higgs boson, which was recently  
 324 observed for the first time by experiments at CERN in 2012. It is electrically  
 325 neutral, has a mass of 125.7  $\pm$  0.4 GeV, and is the only spin-0 particle yet to be  
 326 observed. The Higgs boson is the gauge boson associated with the mechanism  
 327 that gives a mass to the W and Z bosons.

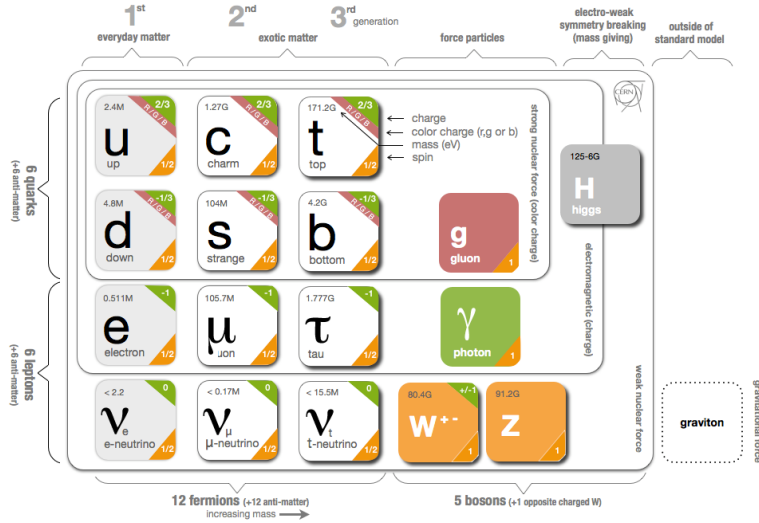


Figure 1: The particle content of the SM.

328 Together these particles form the entire content of the SM, and are summa-  
 329 rized in Figure 1. These are the particles that constitute the observable universe  
 330 and all the so-far-observed interactions within it.

## 331 2.2 INTERACTIONS

332 The interactions predicted and described by the SM are fundamentally tied to the  
 333 particles within it, both in that they describe the way those particles can influence  
 334 each other and also in that the existence of the interactions requires the existence  
 335 of some particles (the gauge bosons).

## 336 2.3 LIMITATIONS

# 3

337

338 SUPERSYMMETRY

---

339 3.1 MOTIVATION

340 3.2 STRUCTURE

341 3.3 PHENOMENOLOGY



# 4

342

343 LONG-LIVED PARTICLES

---

344 4.1 MECHANISMS

345 4.1.1 EXAMPLES IN SUPERSYMMETRY

346 4.2 PHENOMENOLOGY

347 4.2.1 DISIMILARITIES TO PROMPT DECAYS

348 4.2.2 CHARACTERISTIC SIGNATURES



349

### PART III

350

## EXPERIMENTAL STRUCTURE AND RECONSTRUCTION

351

You can put some informational part preamble text here.



# 5

352

353 THE LARGE HADRON COLLIDER

---

354 5.1 INJECTION CHAIN

355 5.2 DESIGN AND PARAMETERS

356 5.3 LUMINOSITY



# 6

357

## 358 THE ATLAS DETECTOR

---

359 6.1 COORDINATE SYSTEM

360 6.2 MAGNETIC FIELD

361 6.3 INNER DETECTOR

362 6.3.1 PIXEL DETECTOR

363 6.3.2 SEMICONDUCTOR TRACKER

364 6.3.3 TRANSITION RADIATION TRACKER

365 6.4 CALORIMETRY

366 6.4.1 ELECTROMAGNETIC CALORIMETERS

367 6.4.2 HADRONIC CALORIMETERS

368 6.4.3 FORWARD CALORIMETERS

369 6.5 MUON SPECTROMETER

370 6.6 TRIGGER

371 6.6.1 TRIGGER SCHEME

372 6.6.2 MISSING TRANSVERSE ENERGY TRIGGERS



# 7

373

## 374 EVENT RECONSTRUCTION

---

375 The ATLAS experiment combines measurements in the subdetectors to form a  
376 cohesive picture of each physics event.

### 377 7.1 TRACKS AND VERTICES

#### 378 7.1.1 TRACK RECONSTRUCTION

##### 379 7.1.1.1 NEURAL NETWORK

##### 380 7.1.1.2 PIXEL DE/DX

#### 381 7.1.2 VERTEX RECONSTRUCTION

### 382 7.2 JETS

#### 383 7.2.1 TOPOLOGICAL CLUSTERING

#### 384 7.2.2 JET ENERGY SCALE

#### 385 7.2.3 JET ENERGY SCALE UNCERTAINTIES

#### 386 7.2.4 JET ENERGY RESOLUTION

### 387 7.3 ELECTRONS

#### 388 7.3.1 ELECTRON IDENTIFICATION

### 389 7.4 MUONS

#### 390 7.4.1 MUON IDENTIFICATION

### 391 7.5 MISSING TRANSVERSE ENERGY



392

## PART IV

393

### CALORIMETER RESPONSE

394

You can put some informational part preamble text here.



# 8

395

## 396 RESPONSE MEASUREMENT WITH SINGLE HADRONS

---

397 As discussed in Section 7.2, colored particles produced in collisions hadronize  
398 into jets of multiple hadrons. One approach to understanding jet energy mea-  
399 surements in the ATLAS calorimeters is to evaluate the calorimeter response to  
400 those individual hadrons; measurements of individual hadrons can be used to  
401 build up an understanding of the jets that they form. The redundancy of the  
402 momentum provided by the tracking system and the energy provided by the  
403 calorimeter provides an opportunity to study calorimeter response using real  
404 collisions, as described further in Section 8.2.

405 Calorimeter response includes a number of physical effects that can be ex-  
406 tracted to provide insight into many aspects of jet modeling. First, many charged  
407 hadrons interact with the material of the detector prior to reaching the calorime-  
408 ters and thus do not deposit any energy. Comparing this effect in data and simu-  
409 lation is a powerful tool in validating the interactions of particles with the mate-  
410 rial of the detector and the model of the detector geometry in simulation, see Sec-  
411 tion 8.2.2. The particles which do reach the calorimeter deposit their energy into  
412 several adjacent cells, which are then clustered together. The energy of the clus-  
413 ter is then the total energy deposited by that particle. Comparing the response of  
414 hadrons in data to that of simulated hadrons provides a direct evaluation of the  
415 showering of hadronic particles and the energy deposited by particles in matter  
(Section 8.2.4).

417 The above studies all use an inclusive selection of charged particles, which are  
418 comprised predominantly of pions, kaons, and (anti)protons. It is also possible to  
419 measure the response to various identified particle types separately to evaluate  
420 the simulated interactions of each particle, particularly at low energies where  
421 differences between species are very relevant. Pions and (anti)protons can be  
422 identified through decays of long-lived particles, in particular  $\Lambda$ ,  $\bar{\Lambda}$ , and  $K_S^0$ , and  
423 then used to measure response as described above. This is discussed in detail in  
424 Section 8.3.

425 The results in this chapter use data collected at 7 and 8 TeV collected in 2010  
426 and 2012, respectively. Both are included as the calorimeter was repaired and  
427 recalibrated between those two data-taking periods. Both sets of data are com-  
428 pared to an updated simulation that includes new physics models provided by  
429 Geant4 [1] and improvements in the detector description [2, 3]. The present  
430 results are published in European Physical Journal C (EPJC) [4] and can be com-  
431 pared to a similar measurement performed in 2009 and 2010 [5], which used the  
432 previous version of the simulation framework [6].

433 8.1 DATASET AND SIMULATION

434 8.1.1 DATA SAMPLES

435 The two datasets used in this chapter are taken from dedicated low-pileup runs  
 436 where the fraction of events with multiple interactions was negligible. These  
 437 datasets are used rather than those containing full-pileup events to facilitate mea-  
 438 surement of isolated hadrons. The 2012 dataset at  $\sqrt{s} = 8$  TeV contains 8 mil-  
 439 lion events and corresponds to an integrated luminosity of  $0.1 \text{ nb}^{-1}$ . The 2010  
 440 dataset at  $\sqrt{s} = 7$  TeV contains 3 million events and corresponds to an inte-  
 441 grated luminosity of  $3.2 \text{ nb}^{-1}$ . The latter dataset was also used for the 2010 re-  
 442 sults [5], but it has since been reanalyzed with an updated reconstruction includ-  
 443 ing the final, best understanding of the detector description for the material and  
 444 alignment from Run 1.

445 8.1.2 SIMULATED SAMPLES

446 The two datasets above are compared to simulated single-, double-, and non-  
 447 diffractive events generated with Pythia8 [7] using the A2 configuration of  
 448 hadronization [8] and the MSTW 2008 parton-distribution function set [9, 10].  
 449 The admixture of the single-, double-, and non-diffractive events uses the default  
 450 relative contributions from Pythia8. The conditions and energies for the two  
 451 simulations are chosen so that they match those of the corresponding dataset.

452 To evaluate the interaction of hadrons with detector material, the simulation  
 453 uses two different collections of hadronic physics models, called physics lists, in  
 454 Geant4 9.4 [11]. The first, QGSP\_BERT, combines the Bertini intra-nuclear  
 455 cascade [12–14] below 9.9 GeV, a parametrized proton inelastic model from 9.5  
 456 to 25 GeV [15], and a quark-gluon string model above 12 GeV [16–20]. The  
 457 second, FTFP\_BERT, combines the Bertini intra-nuclear cascade [12–14] below  
 458 5 GeV and the Fritiof model [21–24] above 4 GeV. In either list, Geant4 en-  
 459 forces a smooth transition between models where multiple models overlap.

460 8.1.3 EVENT SELECTION

461 The event selection for this study is minimal, as the only requirement is selecting  
 462 good-quality events with an isolated track. Such events are triggered by requir-  
 463 ing at least two hits in the minimum-bias trigger scintillators. After trigger, each  
 464 event is required to have exactly one reconstructed vertex, and that vertex is re-  
 465 quired to have four or more associated tracks.

466 The particles which are selected for the response measurements are first iden-  
 467 tified as tracks in the inner detector. The tracks are required to have at least 500  
 468 MeV of transverse momentum. To ensure a reliable momentum measurement,  
 469 these tracks are required to have at least one hit in the pixel detector, six hits in  
 470 the SCT, and small longitudinal and transverse impact parameters with respect  
 471 to the primary vertex [5]. For the majority of the measurements in this chapter,  
 472 the track is additionally required to have 20 hits in the TRT, which significantly

473 reduces the contribution from tracks which undergo nuclear interactions. This  
 474 requirement and its effect is discussed in more detail in Section 8.2.5. In addition,  
 475 tracks are rejected if there is any other reconstructed track which extrapolates  
 476 to the calorimeter within a cone of  $\Delta R = \sqrt{(\Delta\phi)^2 + (\Delta\eta)^2} < 0.4$ . This require-  
 477 ment guarantees that the contamination of energy from nearby charged particles  
 478 is negligible [5].

## 479 8.2 INCLUSIVE HADRON RESPONSE

480 The calorimeter response is more precisely defined as the ratio of the measured  
 481 calorimeter energy to the true energy carried by the particle, although this true  
 482 energy is unknown. For charged particles, however, the inner detector provides  
 483 a very precise measurement of momentum (with uncertainty less than 1%) that  
 484 can be used as a proxy for true energy. The ratio of the energy deposited by  
 485 the charged particle in the calorimeter,  $E$ , to its momentum measured in the  
 486 inner detector  $p$ , forms the calorimeter response measure called  $E/p$ . Though  
 487 the distribution of  $E/p$  contains a number of physical features, this study focuses  
 488 on the trends in two aggregated quantities:  $\langle E/p \rangle$ , the average of  $E/p$  for the  
 489 selected tracks, and the zero fraction, the fraction of tracks with no associated  
 490 energy in the calorimeter for those tracks.

491 The calorimeter energy assigned to a track is defined using clusters. The clus-  
 492 ters are formed using a 4–2–0 algorithm [25] that begins with seeds requiring  
 493 at least 4 times the average calorimeter cell noise. The neighboring cells with  
 494 at least twice that noise threshold are then added to the cluster, and all bound-  
 495 ing cells are then added with no requirement. This algorithm minimizes noise  
 496 contributions through its seeding process, and including the bounding cells im-  
 497 proves the energy resolution [26]. The clusters are associated to a given track  
 498 if they fall within a cone of  $\Delta R = 0.2$  of the extrapolated position of the track,  
 499 which includes about 90% of the energy on average [5]. This construction is il-  
 500 lustrated in Figure 2.

### 501 8.2.1 E/P DISTRIBUTION

502 The  $E/p$  distributions measured in both data and simulation are shown in Fig-  
 503 ure 3 for two example bins of track momentum and for tracks in the central  
 504 region of the detector. These distributions show several important features of  
 505 the  $E/p$  observable. The large content in the bin at  $E = 0$  comes from tracks that  
 506 have no associated cluster, which occurs due to interactions with detector mate-  
 507 rial prior to reaching the calorimeter or the energy deposit being insufficiently  
 508 large to generate a seed, and are discussed in Section 8.2.2. The small negative  
 509 tail also comes from tracks that do not deposit any energy in the calorimeter but  
 510 are randomly associated to a cluster with an energy below the noise threshold.  
 511 The long positive tail above 1.0 comes from the contribution of neutral parti-  
 512 cles. Nearby neutral particles deposit (sometimes large) additional energy in the  
 513 calorimeter but do not produce tracks in the inner detector, so they cannot be  
 514 rejected by the track isolation requirement. Additionally the peak and mean of

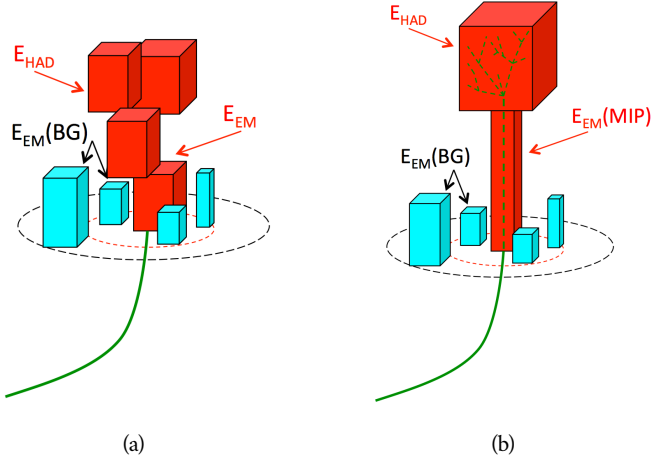


Figure 2: An illustration (a) of the  $E/p$  variable used throughout this paper. The red energy deposits come from the charged particle targeted for measurement, while the blue energy deposits are from nearby neutral particles and must be subtracted. The same diagram (b) for the neutral-background selection, described in Section 8.2.3.

the distribution falls below 1.0 because of the loss of energy not found within the cone as well as the non-compensation of the calorimeter.

The data and simulation share the same features, but the high and low tails are significantly different. The simulated events tend to overestimate the contribution of neutral particles to the long tail, an effect which can be isolated and removed as discussed in Section 8.2.3. Additionally, the simulated clusters have less noise on average, although this is a small effect on the overall response.

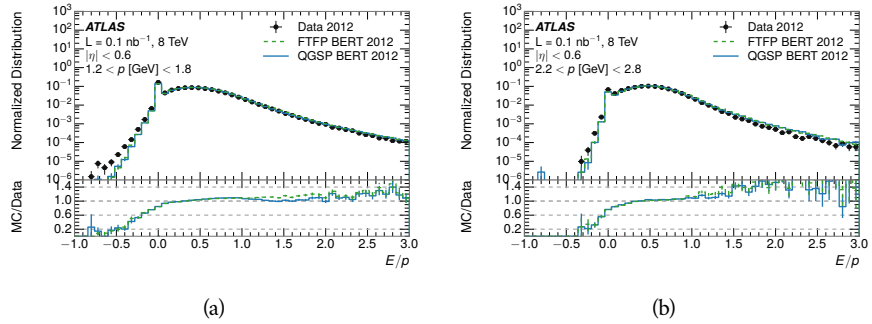


Figure 3: The  $E/p$  distribution and ratio of simulation to data for isolated tracks with (a)  $|\eta| < 0.6$  and  $1.2 < p/\text{GeV} < 1.8$  and (b)  $|\eta| < 0.6$  and  $2.2 < p/\text{GeV} < 2.8$ .

### 8.2.2 ZERO FRACTION

The fraction of particles with no associated clusters, or similarly those with  $E \leq 0$ , reflects the modeling of both the detector geometry and hadronic interactions. The zero fraction is expected to rise as the amount of material a particle traverses

increases, while it is expected to decrease as the particle energy increases. This dependence can be seen in Figure 4, where the zero fraction in data and simulation is shown as a function of momentum and the amount of material measured in interaction lengths. The trends are similar between 2010 and 2012 and for positively and negatively charged particles. The zero fraction decreases with energy as expected. The absolute discrepancy in zero fraction decreases with momentum from 5% to less than 1%, but this becomes more pronounced in the ratio as the zero fraction shrinks quickly with increasing momentum. There is a small constant difference between the data and simulation in both interaction models that becomes more pronounced. The amount of material in the detector increases with  $\eta$ , which is used to obtain results for interaction lengths ranging between 0.1 and 0.65  $\lambda$ . As the data and simulation have significant disagreement in the zero fraction over a number of interaction lengths, the difference must be primarily from the modeling of hadronic interactions with detector material and not just the detector geometry. Although two different hadronic interaction models are shown in the figure, they have very similar discrepancies to data because both use the same description (the BERT model) at low momentum.

### 8.2.3 NEUTRAL BACKGROUND SUBTRACTION

The isolation requirement on hadrons is only effective in removing an energy contribution from nearby charged particles. Nearby neutral particles, predominantly photons from  $\pi^0$  decays, also add their energy to the calorimeter clusters, but mostly in the electromagnetic calorimeter. It is possible to measure this contribution, on average, using late-showering hadrons that minimally ionize in the electromagnetic calorimeter. Such particles are selected by requiring that they deposit less than 1.1 GeV in the EM calorimeter within a cone of  $\Delta R < 0.1$  around the track. To ensure that these particles are well measured, they are additionally required to deposit between 40% and 90% of their energy in the hadronic calorimeter within the same cone.

These particles provide a clean sample to measure the nearby neutral background because they do not deposit energy in the area immediately surrounding them in the EM calorimeter, as shown in Figure 2. So, the energy deposits in the region  $0.1 < \Delta R < 0.2$  can be attributed to neutral particles alone. To estimate the contribution to the whole cone considered for the response measurement, that energy is scaled by a geometric factor of 4/3. This quantity,  $\langle E/p \rangle_{BG}$ , measured in aggregate over a number of particles, gives the contribution to  $\langle E/p \rangle$  from neutral particles in the EM calorimeter. Similar techniques were used in the individual layers of the hadronic calorimeters to show that the background from neutrals is negligible in those layers [5].

The distribution of this background estimate is shown in Figure 5 for data and simulation with the two different physics lists. The contribution from neutral particles falls from 0.1 at low momentum to around 0.03 for particles above 7 GeV. Although the simulation captures the overall trend, it significantly overestimates the neutral contribution for tracks with momentum between 2 and 8 GeV. This effect was also seen in the tails of the  $E/p$  distributions in Figure 3.

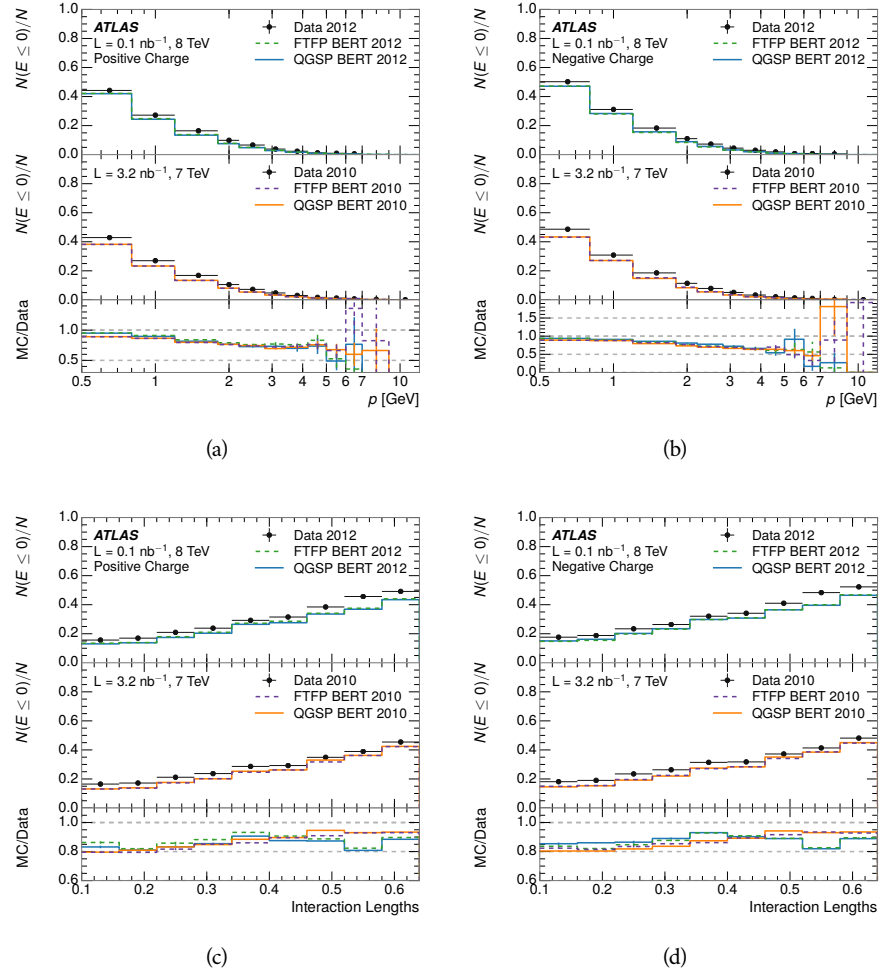


Figure 4: The fraction of tracks as a function (a, b) of momentum, (c, d) of interaction lengths with  $E \leq 0$  for tracks with positive (on the left) and negative (on the right) charge.

570 This difference is likely due to modeling of coherent neutral particle radiation  
 571 in Pythia8 that overestimates the production of  $\pi^0$  near the production of the  
 572 charged particles. The discrepancy does not depend on  $\eta$  and thus is unlikely to  
 573 be a mismodeling of the detector. This difference can be subtracted to form a  
 574 corrected average  $E/p$ , as in Section 8.2.4.

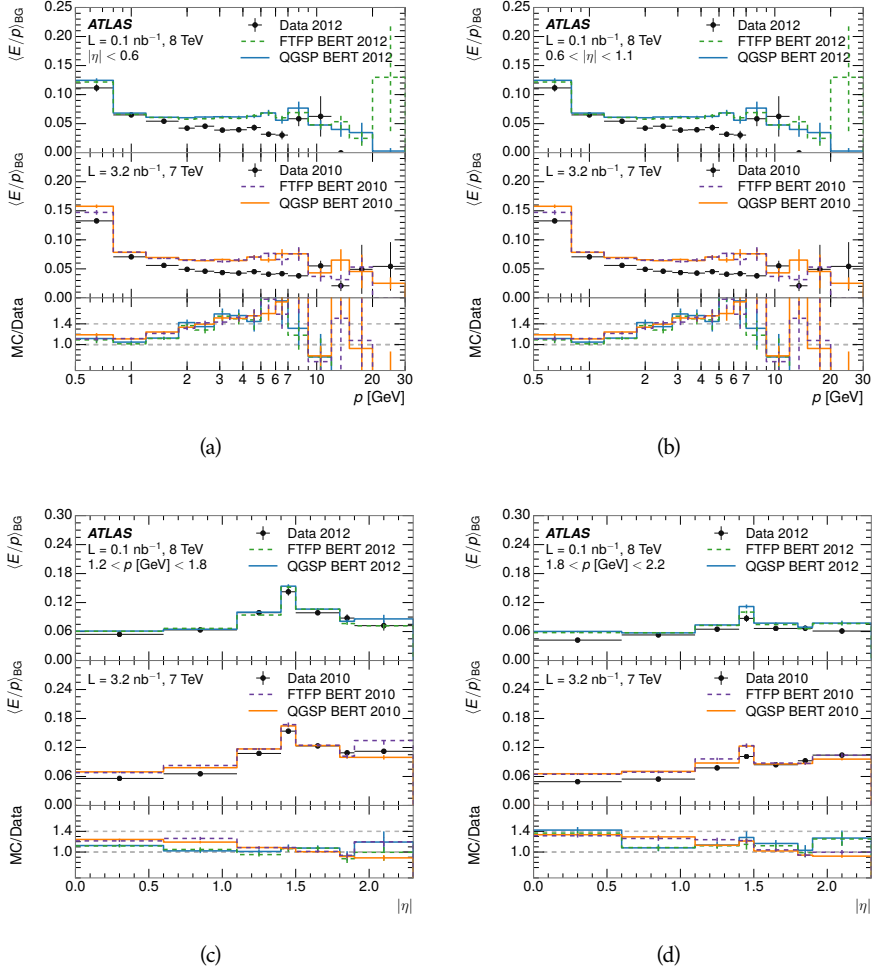


Figure 5:  $\langle E/p \rangle_{\text{BG}}$  as a function of the track momentum for tracks with (a)  $|\eta| < 0.6$ , (b)  $0.6 < |\eta| < 1.1$ , and as a function of the track pseudorapidity for tracks with (c)  $1.2 < p/\text{GeV} < 1.8$ , (d)  $1.8 < p/\text{GeV} < 2.2$ .

#### 575 8.2.4 CORRECTED RESPONSE

576 Figure 6 shows  $\langle E/p \rangle_{\text{COR}}$  as a function of momentum for several bins of pseudo-  
 577 rapidity. This corrected  $\langle E/p \rangle_{\text{COR}} \equiv \langle E/p \rangle - \langle E/p \rangle_{\text{BG}}$  measures the average  
 578 calorimeter response without the contamination of neutral particles. It is the  
 579 most direct measurement of calorimeter response in that it is the energy mea-  
 580 sured for fully isolated hadrons. The correction is performed separately in data  
 581 and simulation, so that the mismodeling of the neutral background in simulation  
 582 is removed from the comparison of response. The simulation overestimates the

583 response at low momentum by about 5%, an effect that can be mostly attributed  
 584 to the underestimation of the zero fraction mentioned previously. For  $|\eta| < 0.6$ ,  
 585 the data-simulation agreement has a larger discrepancy by about 5% for 2010  
 586 than 2012, although this is not reproduced in at higher pseudorapidity.

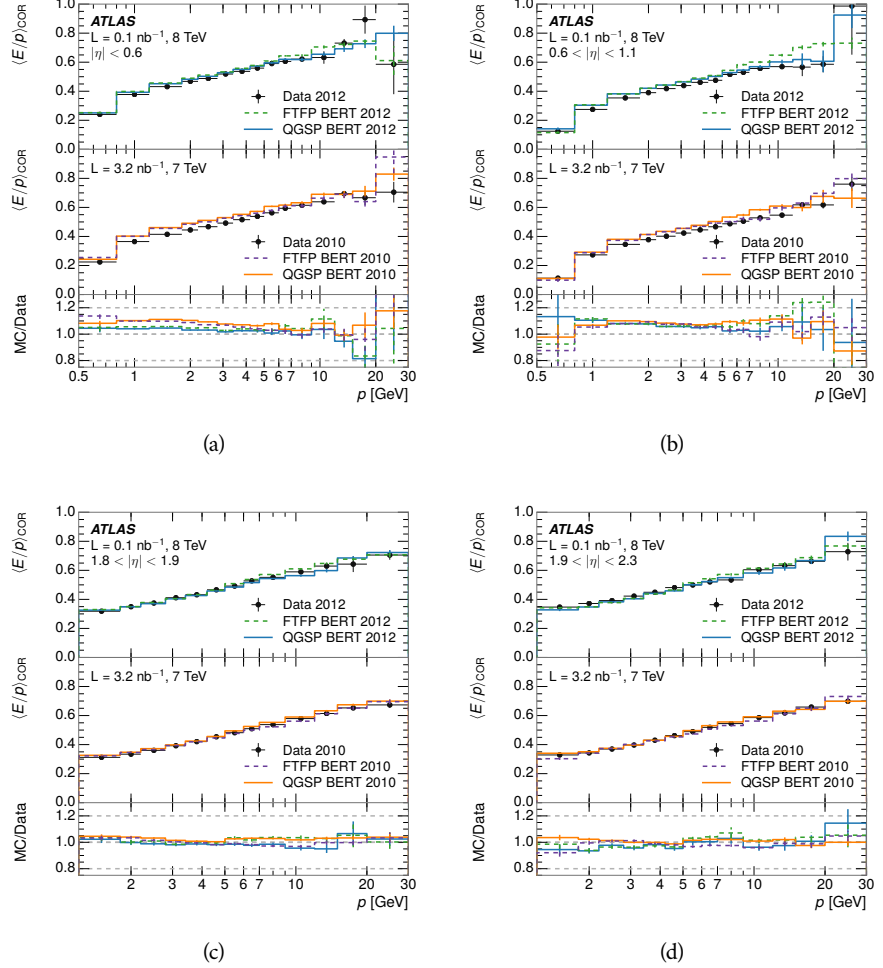


Figure 6:  $\langle E/p \rangle_{\text{COR}}$  as a function of track momentum, for tracks with (a)  $|\eta| < 0.6$ , (b)  $0.6 < |\eta| < 1.1$ , (c)  $1.8 < |\eta| < 1.9$ , and (d)  $1.9 < |\eta| < 2.3$ .

587 The response measurement above used topological clustering at the EM scale,  
 588 that is clusters were formed to measure energy but no corrections were applied  
 589 to correct for expected effects like energy lost outside of the cluster or in unin-  
 590 strumented material. It is also interesting to measure  $\langle E/p \rangle_{\text{COR}}$  using local clus-  
 591 ter weighted ([LCW](#)) energies, which accounts for those effects by calibrating the  
 592 energy based on the properties of the cluster such as energy density and depth in  
 593 the calorimeter. Figure 7 shows these distributions for tracks with zero or more  
 594 clusters and separately for tracks with one or more clusters. The calibration  
 595 moves the mean value of  $\langle E/p \rangle_{\text{COR}}$  significantly closer to 1.0 as desired. The  
 596 agreement between data and simulation improves noticeably when at least one  
 597 cluster is required, as this removes the contribution from the mismodeling of  
 598 the zero fraction. The good agreement in that case again demonstrates that the

difference in  $\langle E/p \rangle_{\text{COR}}$  between data and simulation is caused predominantly by the difference in zero fraction.

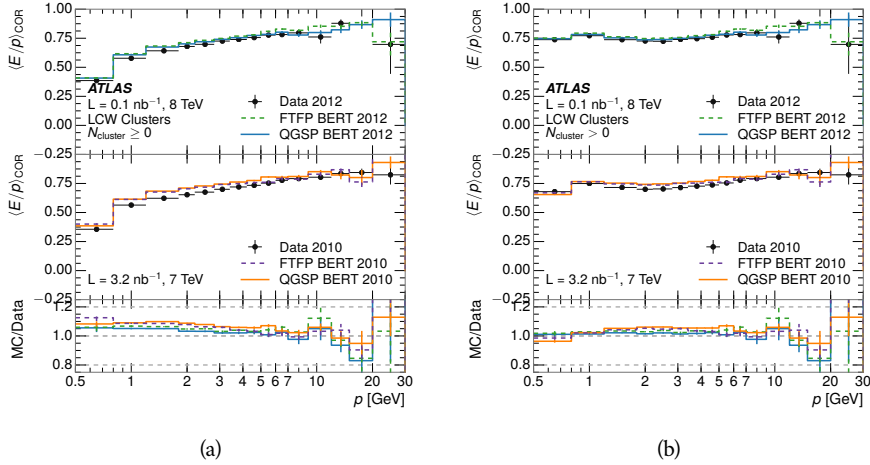


Figure 7:  $\langle E/p \rangle_{\text{COR}}$  calculated using LCW-calibrated topological clusters as a function of track momentum for tracks with (a) zero or more associated topological clusters or (b) one or more associated topological clusters.

## 8.2.5 ADDITIONAL STUDIES

As has been seen in several measurements in previous sections, the simulation does not correctly model the chance of a low momentum hadron to reach the calorimeter. Because of the consistent discrepancy across pseudorapidity and interaction lengths, this can be best explained by incomplete understanding of hadronic interactions with the detector [4]. For example, a hadron that scatters off of a nucleus in the inner detector can be deflected through a significant angle and not reach the expected location in the calorimeter. In addition, these interactions can produce secondary particles that are difficult to model.

The requirement used throughout the previous sections on the number of hits in the TRT reduces these effects by preferentially selecting tracks that do not undergo nuclear interactions. It is interesting to check how well the simulation models tracks with low numbers of TRT hits, which selects tracks that are more likely to have undergone a hadronic interaction. Figure 8 compares the distributions with  $N_{\text{TRT}} < 20$  to  $N_{\text{TRT}} > 20$  for real and simulated particles. As expected, the tracks with fewer hits are poorly modeled in the simulation as  $\langle E/p \rangle_{\text{COR}}$  differs by as much as 25% at low momentum.

Another interesting aspect of the simulation is the description of antiprotons at low momentum, where QGSP\_BERT and FTFP\_BERT have significant differences. This can be seen to have an effect in the inclusive response measurement when separated into positive and negative charge. The  $\langle E/p \rangle_{\text{COR}}$  distributions for positive and negative particles are shown in Figure 9, where a small difference between QGSP\_BERT and FTFP\_BERT can be seen in the distribution for negative tracks. This is demonstrated more clearly in Figure 10, which shows

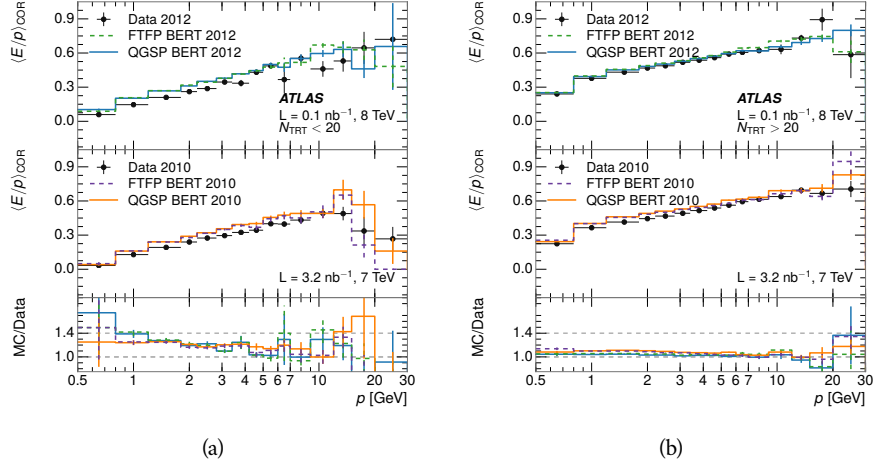


Figure 8: Comparison of the  $\langle E/p \rangle_{\text{COR}}$  for tracks with (a) less than and (b) greater than 20 hits in the TRT.

the  $E/p$  distribution in the two simulations separated by charge. There is a clear difference around  $E/p > 1.0$ , which can be explained by the additional energy deposited by the annihilation of the antiproton in the calorimeter that is modeled well only in FTFP\_BERT. This is also explored with data using identified antiprotons in Section 8.3.

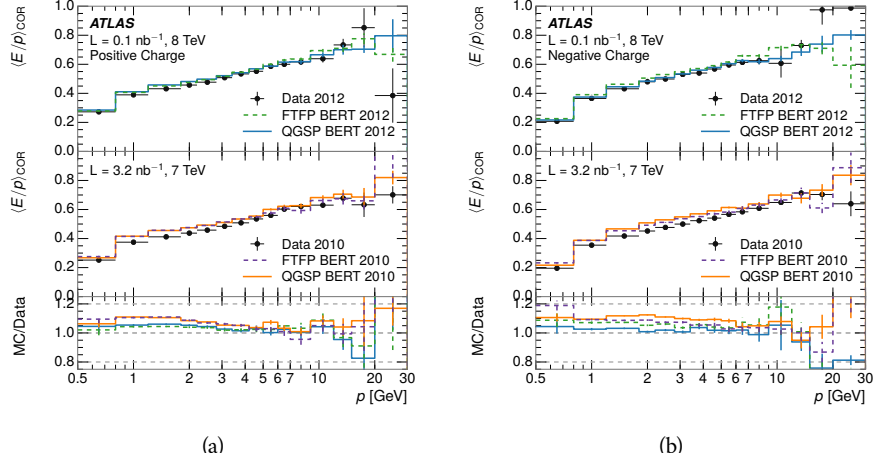


Figure 9: Comparison of the  $\langle E/p \rangle_{\text{COR}}$  for (a) positive and (b) negative tracks as a function of track momentum for tracks with  $|\eta| < 0.6$ .

The  $\langle E/p \rangle$  results in previous sections have considered the electromagnetic and hadronic calorimeters together as a single energy measurement, to emphasize the total energy deposited for a given particle. However, the deposits in each calorimeter are available separately and  $\langle E/p \rangle$  can be constructed for each layer. As the layers are composed of different materials and are modeled separately in the detector geometry, confirmation that the simulation matches the data well

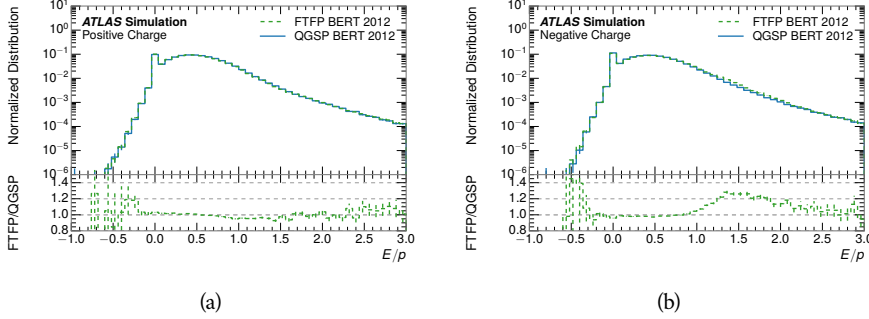


Figure 10: Comparison of the  $E/p$  distributions for (a) positive and (b) negative tracks with  $0.8 < p/\text{GeV} < 1.2$  and  $|\eta| < 0.6$ , in simulation with the FTFP\_BERT and QGSP\_BERT physics lists.

in each layer adds confidence in both the description of hadronic interactions with the two different materials and also the geometric description of each.

The technique discussed in Section 8.2.3 for selecting minimally ionizing particle (MIP)s in the electromagnetic calorimeter is also useful in studying deposits in the hadronic calorimeter. Those MIPs deposit almost all of their energy exclusively in the hadronic calorimeter. Figure 11 shows  $\langle E/p \rangle_{\text{RAW}}^{\text{Had}}$ , where RAW indicates that no correction has been applied for neutral backgrounds and Had indicates that only clusters for the hadronic calorimeter are included. The RAW and COR versions of  $\langle E/p \rangle$  in this case are the same, as the neutral background is negligible in that calorimeter layer. The distributions are shown both for the original EM scale calibration and after LCW calibration. The data and simulation agree very well in this comparison, except in the lowest momentum bin which has 5% discrepancy that has already been seen in similar measurements.

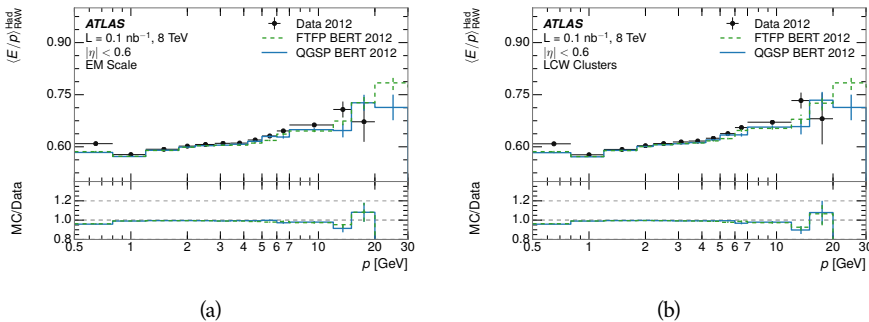


Figure 11: Comparison of the response of the hadronic calorimeter as a function of track momentum (a) at the EM-scale and (b) after the LCW calibration.

A similar comparison can be made in the electromagnetic calorimeter by selecting particles which have no associated energy in the hadronic calorimeter. These results are measured in terms of  $\langle E/p \rangle_{\text{COR}}^{\text{EM}}$ , where EM designates that only clusters in the electromagnetic calorimeter are included and COR designates that the neutral background is subtracted as the neutral background is present in this case. Figure 12 shows the analogous comparisons to Figure 11 in

655 the electromagnetic calorimeter. In this case the disagreement between data and  
 656 simulation is more pronounced, with discrepancies as high as 5% over a larger  
 657 range of momenta. This level of discrepancy indicates that the description of  
 658 the electromagnetic calorimeter is actually the dominant source of discrepancy  
 659 in the combined distributions in Section 8.2.4.

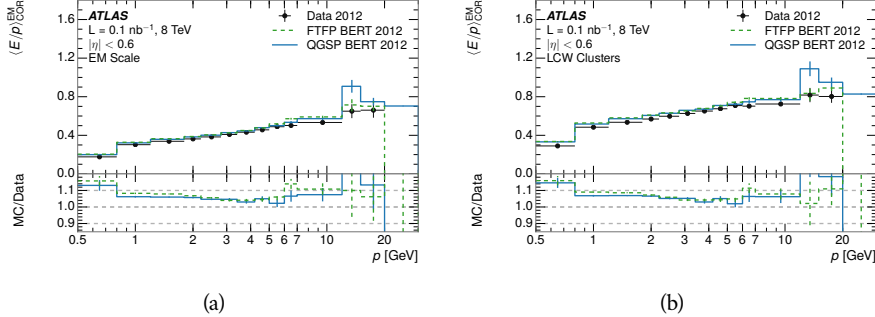


Figure 12: Comparison of the response of the EM calorimeter as a function of track momentum (a) at the EM-scale and (b) with the LCW calibration.

660 **NOTE: There are more studies that I skipped for brevity that could be in-**  
 661 **cluded if interesting.  $E/p$  at different cluster threshold settings,  $E/p$  with**  
 662 **pileup,  $E/p$  with cells. I also left out a lot of eta bins that appear in the**  
 663 **paper so that this section didn't turn into 20 pages of plots.**

### 664 8.3 IDENTIFIED PARTICLE RESPONSE

665 The inclusive response measurement for hadrons can be augmented by measur-  
 666 ing the response for specific particle species. The simulation models each parti-  
 667 cle type separately, and understanding the properties of each is important in con-  
 668 straining the uncertainty on jets. In order to select and measure specific hadrons,  
 669 this section relies on the displaced decays of long-lived particles. Such decays  
 670 can be identified by reconstructing secondary vertices with a requirement on  
 671 mass. In particular,  $\Lambda$ ,  $\bar{\Lambda}$ , and  $K_S^0$  can be used to select a pure sample of protons,  
 672 antiprotons, and pions, respectively.

#### 673 8.3.1 DECAY RECONSTRUCTION

674 The measurement of response for identified particles uses the same selection as  
 675 for inclusive particles (Section 8.1.3) with a few additions. Each event used is  
 676 required to have at least one secondary vertex, and the tracks are required to  
 677 match to that vertex rather than the primary vertex. Pions are selected from  
 678 decays of  $K_S^0 \rightarrow \pi^+ \pi^-$ , which is the dominant decay for  $K_S^0$  to charged particles.  
 679 Protons are selected from decays of  $\Lambda \rightarrow \pi^- p$  and antiprotons from  $\bar{\Lambda} \rightarrow \pi^+ \bar{p}$ ,  
 680 which are similarly the dominant decays of  $\Lambda$  and  $\bar{\Lambda}$  to charged particles. The  
 681 species of parent hadron in these decays is determined by reconstructing the  
 682 mass of the tracks associated to the secondary vertex. The sign of the higher

683 momentum decay particle can distinguish between  $\Lambda$  and  $\bar{\Lambda}$ , which of course  
 684 have the same mass, as the proton or antiproton is kinematically favored to have  
 685 higher momentum. Examples of the reconstructed masses used to select these  
 686 decays are shown in Figure 13.

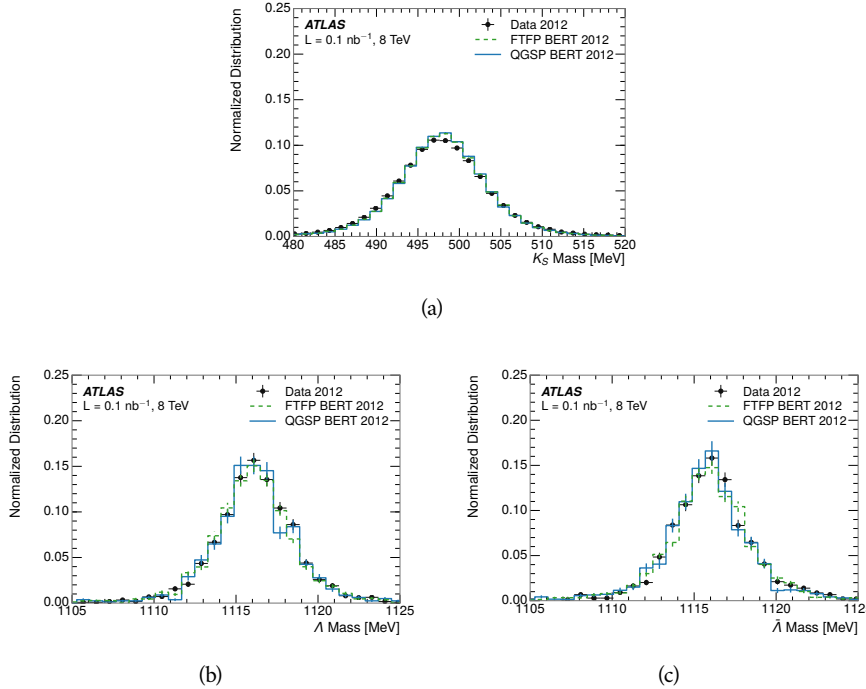


Figure 13: The reconstructed mass peaks of (a)  $K_S^0$ , (b)  $\Lambda$ , and (c)  $\bar{\Lambda}$  candidates.

687 The dominant backgrounds for the identified particle decays are nuclear in-  
 688 teractions and combinatoric sources. These are suppressed by the kinematic re-  
 689 quirements on the tracks as well as an additional veto which removes candidates  
 690 that are consistent with both a  $\Lambda$  or  $\bar{\Lambda}$  and a  $K_S^0$  hypothesis, which is possible be-  
 691 cause of the different assumptions on particle mass in each case [5]. After these  
 692 requirements, the backgrounds are found to be negligible compared to the sta-  
 693 tistical errors on these measurements.

### 694 8.3.2 IDENTIFIED RESPONSE

695 With these techniques the  $E/p$  distributions are extracted in data and simulation  
 696 for each particle species and shown in Figure 14. These distributions are shown  
 697 for a particular bin of  $E_a$  ( $2.2 < E_a/\text{GeV} < 2.8$ ), rather than  $p$ .  $E_a$  is the energy  
 698 available to be deposited in the calorimeter: for pions  $E_a = \sqrt{p^2 + m^2}$ , for pro-  
 699 tons  $E_a = \sqrt{p^2 + m^2} - m$ , and for antiprotons  $E_a = \sqrt{p^2 + m^2} + m$ . The features  
 700 of the  $E/p$  distributions are similar to the inclusive case. There is a small nega-  
 701 tive tail from noise and a large fraction of tracks with zero energy from particles  
 702 which do not reach the calorimeter. The long positive tail is noticeably more  
 703 pronounced for antiprotons because of the additional energy generated by the  
 704 annihilation in addition to the neutral background.

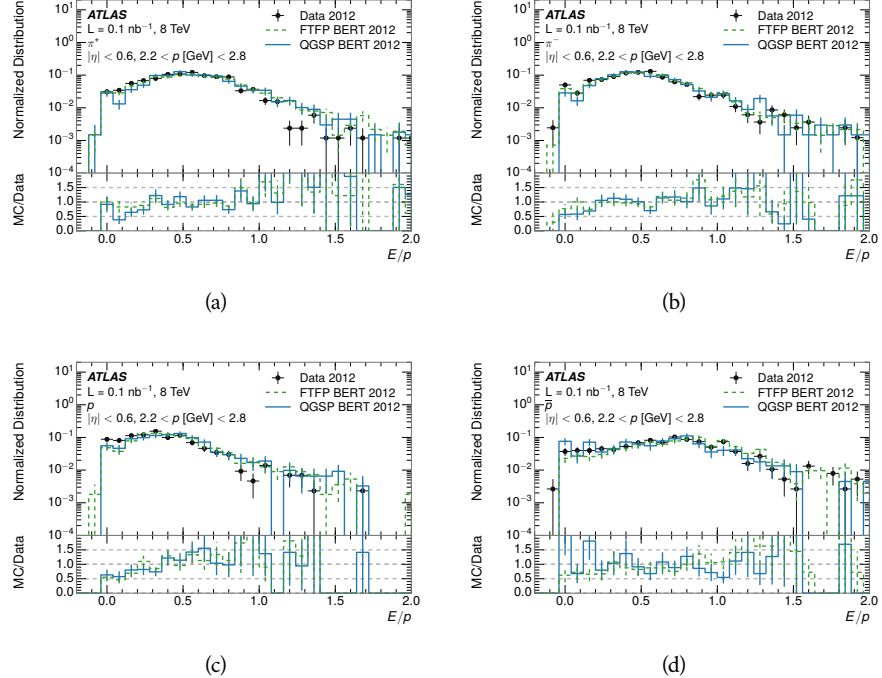


Figure 14: The  $E/p$  distribution for isolated (a)  $\pi^+$ , (b)  $\pi^-$ , (c) proton, and (d) anti-proton tracks.

705     The zero fraction is further explored in Figure 15 for pions and protons in data  
 706     and simulation. The simulation consistently underestimates the zero fraction  
 707     independent of particle species, which implies that this discrepancy is not caused  
 708     by the model of a particular species but rather a feature common to all.

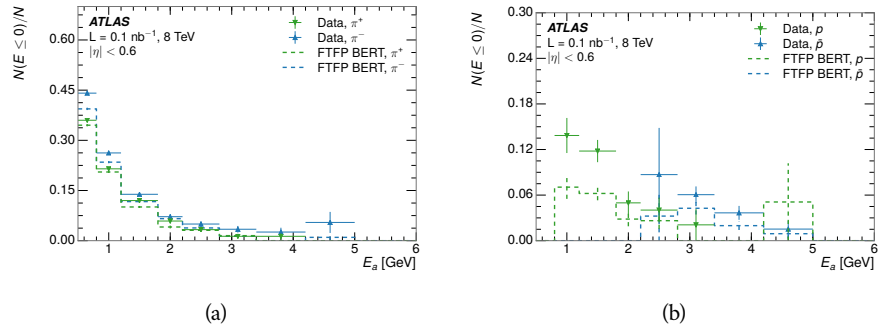


Figure 15: The fraction of tracks with  $E \leq 0$  for identified (a)  $\pi^+$  and  $\pi^-$ , and (b) proton and anti-proton tracks

709     It is also interesting to compare the response between the different particle  
 710     species. One approach to do this is to measure the difference in  $\langle E/p \rangle$  between  
 711     two types, which has the advantage of removing the neutral background. These  
 712     differences are shown in various combinations in Figure 16. The response for  
 713      $\pi^+$  is greater on average than the response to  $\pi^-$  because of a charge-exchange  
 714     effect which causes the production of additional neutral pions in the showers of

715  $\pi^+$  [27]. The response for  $\pi^+$  is also greater on average than the response to  $p$ ,  
 716 because a large fraction of the energy of  $\pi^+$  hadrons is converted to an electro-  
 717 magnetic shower [28, 29]. However, the  $\bar{p}$  response is significantly higher than  
 718 the response to  $\pi^-$  because of the annihilation of the antiproton. FTFP\_BERT  
 719 does a better job of modeling this effect than QGSP\_BERT because of their differ-  
 720 ent descriptions of  $\bar{p}$  interactions with material.

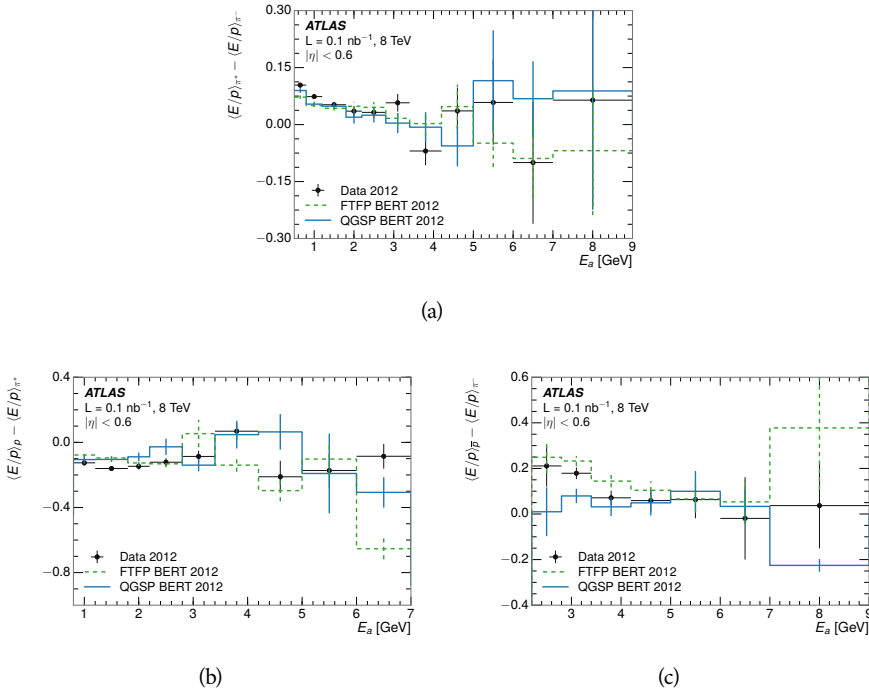


Figure 16: The difference in  $\langle E/p \rangle$  between (a)  $\pi^+$  and  $\pi^-$  (b)  $p$  and  $\pi^+$ , and (c)  $\bar{p}$  and  $\pi^-$ .

721 It is also possible to remove the neutral background from these response dis-  
 722 tributions using the same technique as in Section 8.2.3. The technique is largely  
 723 independent of the particle species and so can be directly applied to  $\langle E/p \rangle$  for  
 724 pions. The  $\langle E/p \rangle_{\text{COR}}$  distributions for pions are shown in Figure 17, which are  
 725 very similar to the inclusive results. The inclusive hadrons are comprised mostly  
 726 of pions, so this similarity is not surprising. It is also possible to see the small  
 727 differences between  $\pi^+$  and  $\pi^-$  response here, where  $\langle E/p \rangle_{\text{COR}}$  is higher on av-  
 728 erage for  $\pi^+$ . The agreement between data and simulation is significantly worse  
 729 for the  $\pi^-$  distributions than for the  $\pi^+$ , with a discrepancy greater than 10%  
 730 below 2-3 GeV.

### 731 8.3.3 ADDITIONAL SPECIES IN SIMULATION

732 The techniques above provide a method to measure the response separately for  
 733 only pions and protons. However the hadrons which forms jets include a num-  
 734 ber of additional species such as kaons and neutrons. The charged kaons are  
 735 an important component of the inclusive charged hadron distribution, which is  
 736 comprised of roughly 60-70% pions, 15-20% kaons, and 5-15% protons. These

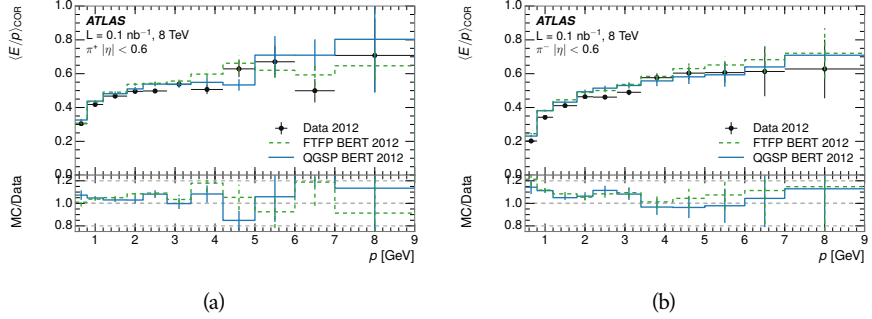


Figure 17:  $\langle E/p \rangle_{\text{COR}}$  as a function of track momentum for (a)  $\pi^+$  tracks and (b)  $\pi^-$  tracks.

are difficult to measure in data at the ATLAS detector, although a template subtraction technique has been proposed which may be effective with larger sample sizes [4]. The simulation of these particles includes noticeable differences in response at low energies, which are shown in Figure 18 for FTFP\_BERT. The significant differences in response between low energy protons and antiprotons are accounted for above in the definitions of  $E_a$ .

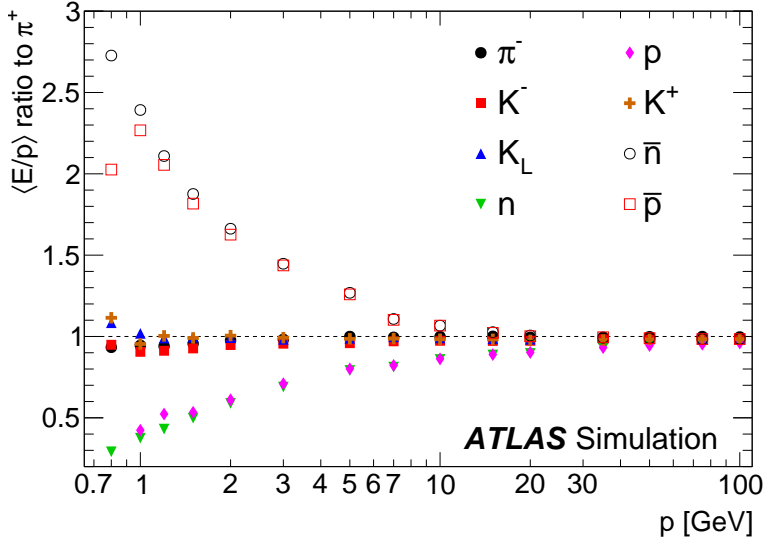


Figure 18: The ratio of the calorimeter response to single particles of various species to the calorimeter response to  $\pi^+$  with the physics list FTFP\_BERT.

#### 8.4 SUMMARY

These various measurements of calorimeter response shown above for data and simulation illuminate the accuracy of the simulation of hadronic interactions at the ATLAS detector. The results were done using 2010 and 2012 data at 7 and 8 TeV, but reflect the most current understanding of the detector alignment and geometry. A number of measurements focusing on a comparison between pro-

749 tons and antiprotons suggest that FTFP\_BERT models those interaction more  
750 accurately than QGSP\_BERT. These measurements, among others, were the moti-  
751 vation to switch the default Geant4 simulation from FTFP\_BERT to QGSP\_BERT  
752 for all ATLAS samples.

753 Even with these updates, there are a number of small, approximately 5%, dis-  
754 crepancies in response between the data and simulation at low energies. At  
755 higher energies the simulation of hadronic interactions is very consistent with  
756 data. Chapter 9 discusses how to use these observed differences to constrain the  
757 jet energy scale and its associated uncertainties.



758

## 759 JET ENERGY RESPONSE AND UNCERTAINTY

## 760 9.1 MOTIVATION

761 As jets form a major component of many physics analyses at ATLAS, it is cru-  
 762 cial to carefully calibrate the measurement of jet energies and to derive an un-  
 763 certainty on that measurement. These uncertainties have often been the dom-  
 764 inant systematic uncertainty in high-energy analyses at the Large Hadron Col-  
 765 linder ([LHC](#)). Dijet and multijet balance techniques provide a method to constrain  
 766 the [JES](#) and its uncertainty in data, and provide the default values used for ATLAS  
 767 jet measurements at most energies [30]. These techniques are limited by their re-  
 768 liance on measuring jets in data, so they are statistically limited in estimating  
 769 the jet energy scale at the highest jet energies. This chapter presents another  
 770 method for estimating the jet energy scale and its uncertainty which builds up a  
 771 jet from its components and thus can be naturally extended to high jet momen-  
 772 tum. Throughout this chapter the jets studied are simulated using [Pythia8](#) with  
 773 the CT10 parton distribution set [31] and the AU2 tune [8], and corrections are  
 774 taken from the studies including data and simulation in Chapter 8.

775 As described in Section 7.2, jets are formed from topological clusters of energy  
 776 in the calorimeters using the anti- $k_t$  algorithm. These clusters originate from a  
 777 diverse spectrum of particles, in terms of both species and momentum, leading to  
 778 significantly varied jet properties and response between jets of similar produced  
 779 momentum. Figure 19 shows the simulated distribution of particles within jets  
 780 at a few examples energies. The  $E/p$  measurements provide a thorough under-  
 781 standing of the dominant particle content of jets, the charged hadrons.

## 782 9.2 UNCERTAINTY ESTIMATE

783 Simulated jets are not necessarily expected to correctly model the energy de-  
 784 posits in the calorimeters, because of the various discrepancies discussed in Chap-  
 785 ter 8. To evaluate a jet energy response, the simulated jet energies are compared  
 786 to a corrected jet built up at the particle level. Each cluster in a jet is associated  
 787 to the truth particle which deposited it, and the energy in that cluster is then  
 788 corrected for a number of effects based on measurements in data. The primary  
 789 corrections come from the single hadron response measurements in addition  
 790 to response measured using the combined test beam which covers higher mo-  
 791 mentum particles [32]. These corrections include both a shift ( $\Delta$ ), in order to  
 792 make the simulation match the average response in data, and an uncertainty ( $\sigma$ )  
 793 associated with the ability to constrain the difference between data and simula-  
 794 tion. Some of the dominant sources of uncertainty are itemized in Table 1 with  
 795 typical values, and the full list considered is described in detail in the associated

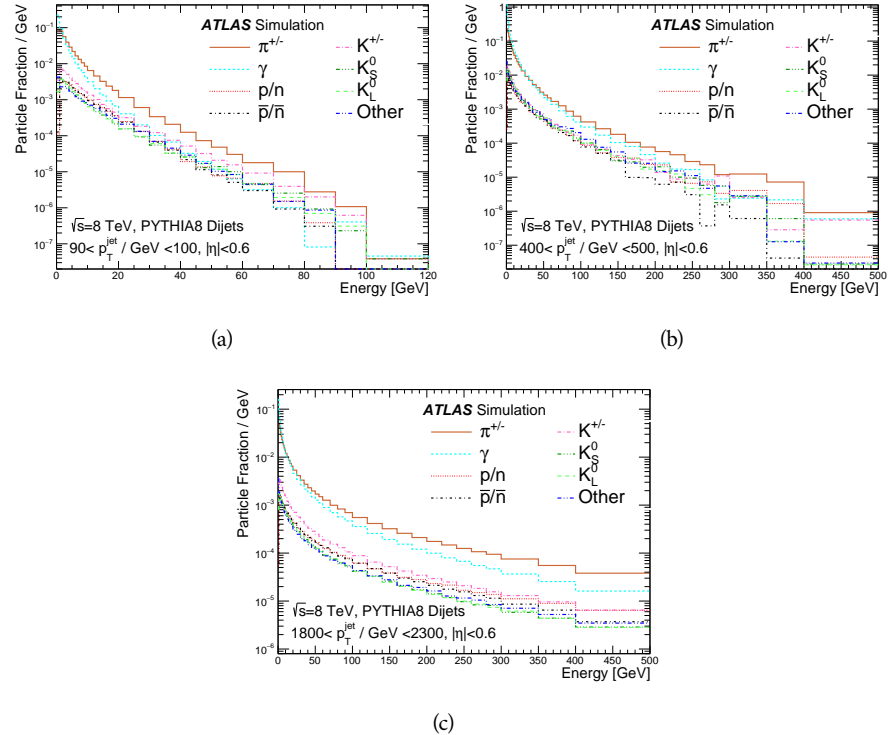


Figure 19: The spectra of true particles inside anti- $k_t$ ,  $R = 0.4$  jets with (a)  $90 < p_T/\text{GeV} < 100$ , (b)  $400 < p_T/\text{GeV} < 500$ , and (c)  $1800 < p_T/\text{GeV} < 2300$ .

paper [4]. These uncertainties cover differences between the data and simulation in the modeling of calorimeter response to a given particle. No uncertainties are added for the difference between particle composition of jets in data and simulation.

From these terms, the jet energy scale and uncertainty is built up from individual energy deposits in simulation. Each uncertainty term is treated independently, and are taken to be gaussian distributed. The resulting scale and uncertainty is shown in Figure 20, where the mean response is measured relative to the calibrated energy reported by simulation. The dominant uncertainties come from the statistical uncertainties on the  $E/p$  measurements at lower energies and the additional uncertainty for out of range measurements at higher energies. The total uncertainty from this method at intermediate jet energies is comparable to other simulation-based methods [33] and is about twice as large as in-situ methods using data [30]. This method is the only one which provides an estimation above 1.8 TeV, however, and so is still a crucial technique in analyses that search for very energetic jets.

These techniques can also be used to measure the correlation between bins of average reconstructed jet momentum across a range of  $p_T$  and  $|\eta|$ , where correlations are expected because of a similarity in particle composition at similar energies. Figure 21 shows these correlations, where the uncertainties on jets in neighboring bins are typically between 30% and 60% correlated. The uncertainty on all jets becomes significantly correlated at high energies and larger pseudora-

Abbrev.	Description	$\Delta$ (%)	$\sigma$ (%)
In situ $E/p$	The comparison of $\langle E/p \rangle_{\text{COR}}$ as described in Chapter 8 with statistical uncertainties from 500 MeV to 20 GeV.	0-3	1-5
CTB	The main $\langle E/p \rangle$ comparison uncertainties, binned in $p$ and $ \eta $ , as derived from the combined test beam results, from 20 to 350 GeV [32].	0-3	1-5
$E/p$ Zero Fraction	The difference in the zero-fraction between data and MC simulation from 500 MeV to 20 GeV.	5-25	1-5
$E/p$ Threshold	The uncertainty in the EM calorimeter response from the potential mismodeling of threshold effects in topological clustering.	0	0-10
Neutral	The uncertainty in the calorimeter response to neutral hadrons based on studies of physics model variations.	0	5-10
$K_L$	An additional uncertainty in the response to neutral $K_L$ in the calorimeter based on studies of physics model variations.	0	20
$E/p$ Misalignment	The uncertainty in the $p$ measurement from misalignment of the ID.	0	1
Hadrons, $p > 350$ GeV	A flat uncertainty for all particles above the energy range or outside the longitudinal range probed with the combined test beam.	0	10

Table 1: The dominant sources of corrections and systematic uncertainties in the [JES](#) estimation technique, including typical values for the correcting shift ( $\Delta$ ) and the associated uncertainty ( $\sigma$ ).

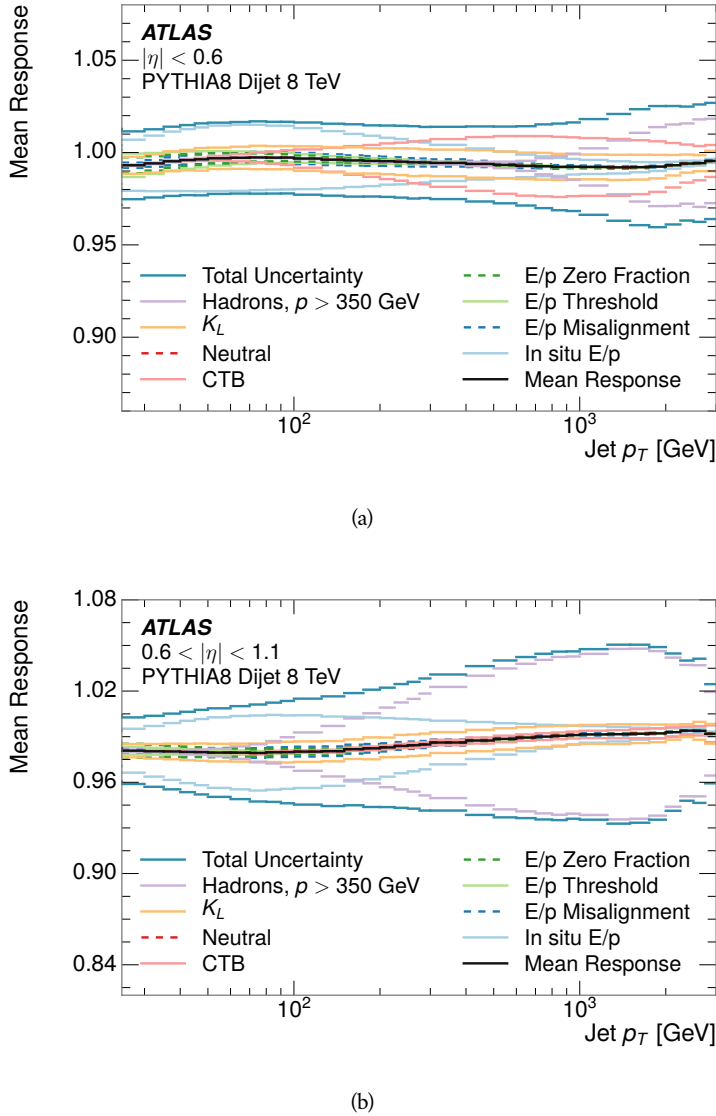


Figure 20: The [JES](#) uncertainty contributions, as well as the total [JES](#) uncertainty, as a function of jet  $p_T$  for (a)  $|\eta| < 0.6$  and (b)  $0.6 < |\eta| < 1.1$ .

818      pidities, when the uncertainty becomes dominated by the single term reflecting  
 819      out of range particles.

### 820      9.3 SUMMARY

821      The technique described above provides a jet energy scale and uncertainty by  
 822      building up jet corrections from the energy deposits of constituent particles. The  
 823       $E/p$  measurements are crucial in providing corrections for the majority of parti-  
 824      cles in the jets. The uncertainty derived this way is between 2 and 5% and is about  
 825      twice as large at corresponding momentum than jet balance methods. However  
 826      this is the only uncertainty available for very energetic jets using 2012 data and  
 827      simulation, and repeating this method with Run 2 data and simulation will be

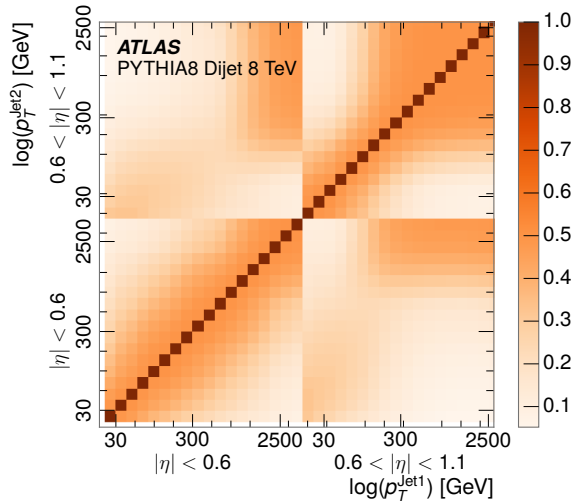


Figure 21: The JES correlations as a function of jet  $p_T$  and  $|\eta|$  for jets in the central region of the detector.

828 important in providing an uncertainty for the most energetic jets in 13 TeV col-  
 829 lisions.



830

## PART V

831

### SEARCH FOR LONG-LIVED PARTICLES

832

You can put some informational part preamble text here.



835 As discussed in Section 2.3, various limitations in the SM suggest a need for new  
 836 particles at the TeV scale. A wide range of extensions to the Standard Model  
 837 predict that these new particles can have lifetimes greater than approximately  
 838 one-hundredth of a nanosecond. These include theories with universal extra-  
 839 dimensions [34, 35], with new fermions [36], and with leptoquarks [37]. Many  
 840 Supersymmetry (SUSY) theories also produce these Long-Lived Particles (LLPs),  
 841 in both R-Parity violating [38–40] and R-Parity conserving [41–44] formula-  
 842 tions. Split supersymmetry [45, 46], for example, predicts long-lived gluinos  
 843 with O(TeV) masses. This search focuses specifically on the SUSY case, but many  
 844 of the results are generic to any model with LLPs.

845 Long-lived gluinos or squarks carry color-charge and will thus hadronize into  
 846 color neutral bound states called R-Hadrons. These are composit particles like  
 847 the usual hadrons but with one supersymmetric constituent, for example  $\tilde{g}q\bar{q}$   
 848 and  $\tilde{q}\bar{q}$ . Through this hadronization process, the neutral gluino can acquire a  
 849 charge. Gluino pair production,  $pp \rightarrow \tilde{g}\tilde{g}$  has the largest cross sectional in-  
 850 crease with the increase in energy to 13 TeV, and so this search focuses on gluino  
 851 R-Hadrons. Planned future updates will extend the case to explicitly included  
 852 squark and chargino models, but the method covers any long-lived, charged,  
 853 massive particle.

## 854 10.1 EVENT TOPOLOGY

855 The majority of SUSY models predict that gluinos will be produced in pairs at  
 856 the LHC, through processes like  $pp \rightarrow q\bar{q} \rightarrow \tilde{g}\tilde{g}$  and  $pp \rightarrow gg \rightarrow \tilde{g}\tilde{g}$ , where the  
 857 gluon mode dominates for the collision energy and gluino masses considered  
 858 for this search. During their production, the long-lived gluinos hadronize into  
 859 color singlet bound states including  $\tilde{g}q\bar{q}$ ,  $\tilde{g}qqq$ , and even  $\tilde{g}g$  [47]. The probability  
 860 to form the gluon-only bound states is a free parameter usually taken to be 0.1,  
 861 while the meson states are favored among the R-Hadrons [48]. The charged and  
 862 neutral states are approximately equally likely for mesons, so the R-Hadrons will  
 863 be charged roughly 50% of the time.

864 These channels produce R-Hadrons with large  $p_T$ , comparable to their mass,  
 865 so that they typically propagate with  $0.2 < \beta < 0.9$  [48]. The fragmentation that  
 866 produces that hadrons is very hard, so the jet structure around the R-Hadron  
 867 is minimal, with less than 5 GeV of summed particle momentum expected in a  
 868 cone of  $\Delta R < 0.25$  around the R-Hadron [48]. After hadronization, depending  
 869 on the gluino lifetime, the R-Hadrons then decay into hadrons and a Lightest  
 870 Supersymmetric Particle (LSP) [47].

871 In summary, the expected event for pair-produced long-lived gluinos is very  
 872 simple: two isolated, high-momentum R-Hadrons that propagate through the

873 detector before decaying to jets. The observable features of such events depend  
 874 strongly on the interaction of the R-Hadron with the material of the detector and  
 875 also its lifetime. Section 10.1.1 describes the interactions of R-Hadrons which  
 876 reach the various detector elements in A Toroidal LHC ApparatuS ([ATLAS](#)) and  
 877 Section 10.1.2 provides a summary of the observable event descriptions for R-  
 878 Hadrons of various lifetimes.

879 10.1.1 DETECTOR INTERACTIONS

880 After approximately 0.2 ns, the R-Hadron reaches the pixel detector. Because  
 881 of its comparatively low  $\beta$ , it heavily ionizes in the silicon if charged, according  
 882 to the Bethe equation [49]. This large ionization can be measured through time  
 883 over threshold (ToT) as described in Section 7.1.1.2. The large ionization is one  
 884 characteristic feature of LLPs.

885 Throughout the next few nanoseconds, the R-Hadron propagates through the  
 886 remainder of the inner detector. A charged R-Hadron will provide hits in each  
 887 of these systems as would any other charged particle, and can be reconstructed  
 888 as a track. The track reconstruction provides a measurement of its trajectory  
 889 and thus its momentum as described in Section 7.1. **Note: At this point I am**  
 890 **failing to mention that the TRT provides a possible dE/dx measurement,**  
 891 **because no one uses it as far as I know.**

892 As of roughly 20 ns, the R-Hadron enters the calorimeter where it interacts  
 893 hadronically with the material. Because of its large mass and momentum, the  
 894 R-Hadron does not typically stop in the calorimeter, but rather deposits energy  
 895 through repeated interactions. Each of these interactions can potentially change  
 896 its quark content and thus change the sign of the R-Hadron, so that the charge  
 897 at exit is typically uncorrelated with the charge at entry [48]. The total energy  
 898 deposited in the calorimeters during the propagation is small compared to the  
 899 kinetic energy of the R-Hadron, around 20-40 GeV, so that  $E/p$  is typically less  
 900 than 0.1 [48].

901 Then, 30 ns after the collision, it reaches the muon system, where it can be  
 902 reconstructed as a muon track. Because of the charge-flipping interactions in  
 903 the calorimeter, this track may have the opposite sign of the track reconstructed  
 904 in the inner detector, or there may be a track present when there was none in  
 905 the inner detector and vice-versa. The propagation time at the characteristically  
 906 lower  $\beta$  results in a significant delay compared to muons, and that delay can be  
 907 assessed in terms of a time-of-flight measurement. Because of the probability of  
 908 charge-flip and late arrival, there is a significant chance that an R-Hadron which  
 909 was produced with a charge will not be identified as a muon.

910 10.1.2 LIFETIME DEPENDENCE

911 The above description assumed a lifetime long enough for the R-Hadron to exit  
 912 the detector, which through this search is referred to as “stable”, even though  
 913 the particle may decay after exiting the detector. There are several unique sig-

natures at shorter lifetimes where the R-Hadron decays in various parts of the inner detector; these lifetimes are referred to as “metastable”.

The shortest case where the R-Hadron is considered metastable is for lifetimes around 0.01 ns, where the particle decays before reaching any of the detector elements. Although the R-Hadrons are produced opposite each other in the transverse plane, each R-Hadron decays to a jet and an LSP which can result in large missing energy. Additionally, the precision of the tracking system allows the displaced vertex of the R-Hadron decay to be reconstructed from the charged particles in the jet. Previous searches on ATLAS have used the displaced vertex to target LLP decays [50].

The next distinguishable case occurs at lifetimes greater than 0.1 ns, where the R-Hadron forms a partial track in the inner detector. If the decay products are sufficiently soft, they may not be reconstructed, and this forms a unique signature of a disappearing track. A dedicated search on ATLAS used the disappearing track signature to search for LLP in Run 1 [51]. **Note: might not be worth mentioning the disappearing track here since it is actually a chargino search, the soft pion is pretty unique to charginos.**

If the decay products are not soft, the R-Hadron daughters form jets, resulting in an event-level signature of up to two high-momentum tracks, jets, and significant missing energy. The missing energy has the same origin as in the case of 0.01 ns lifetimes, from the decay to unmeasured particles, and can be large. The high-momentum tracks will also have the characteristicly high-ionization of massive, long-lived paticles in the inner detector. Several previous searches on ATLAS from Run 1 have used this signature to search for R-Hadrons [52, 53], including a dedicated search for metastable particles [54].

If the lifetime is longer than a few nanoseconds, in the range of 30-50 ns, the R-Hadron decay can occur in or after the calorimeters, but prior to reaching the muon system. This case is similar to the above, although the jets may not be reconstructed, and is covered in the same search strategies. The events still often have large missing energy, although it is generated through different mechanisms. The R-Hadrons do not deposit much energy in the calorimeters, so a neutral R-Hadron will not enter into the missing energy calculation. A charged R-Hadron opposite a neutral R-Hadron will thus generate significant missing energy, and close to 50% of pair-produced R-Hadron events fall into this category. If both R-Hadrons are neutral then the missing energy will be low because neither is detected. Two charged R-Hadrons will also result in low missing energy because both are reconstructed as tracks and will balance each other in the transverse plane. A small fraction of the time, one of the charged R-Hadron tracks may fail quality requirements and thus be excluded from the missing energy calculation and again result in signficant missing energy.

The longest lifetimes, the stable case, has all of the features of the 30-50 ns case but with the addition of muon tracks for any R-Hadrons that exit the calorimeter with a charge. That muon track can provide additional information from time-of-flight measurements to help identify LLPs. Some searches on ATLAS have included this information to improve the search reach for stable particles [53, 55].

959 10.2 SIMULATION

960

961 EVENT SELECTION

---

962 The [LLPs](#) targeted by this search differ in their interactions with the detector from  
 963 [SM](#) particles primarily because of their large mass. When produced at the energies  
 964 available at the [LHC](#), that large mass results in a low  $\beta$ . Such slow-moving  
 965 particles heavily ionize in detector material. Each layer of the pixel detector pro-  
 966 vides a measurement of that ionization, through [ToT](#), as discussed in Section 6.3.1.  
 967 The ionization in the pixel detector, quantified in terms of  $dE/dx$ , provides the  
 968 major focus for this search technique. It is effective both for its discriminating  
 969 power and also because of the large range of lifetimes where it can be used. How-  
 970 ever  $dE/dx$  needs to be augmented with a few additional selection requirements  
 971 to form a complete search.

972 Ionization is not currently available in any form during triggering, so this  
 973 search instead relies on  $E_T^{\text{miss}}$  to trigger signal events. Although triggering on  
 974  $E_T^{\text{miss}}$  can be inefficient,  $E_T^{\text{miss}}$  is often large for many production mechanisms  
 975 of [LLPs](#), as discussed in Section 10.1.

976 Ionization is most effective in rejecting backgrounds for well-measured, high-  
 977 momentum tracks, so some basic requirements on quality and kinematics are  
 978 placed on the particles considered in this search. In particular a newly intro-  
 979 duced tracking variable is very effective in removing highly-ionizing backgrounds  
 980 caused by overlapping tracks. A few additional requirements are placed on the  
 981 tracks considered for [LLP](#) candidates that increase background rejection by tar-  
 982 geting specific types of [SM](#) particles. These techniques provide a significant anal-  
 983 ysis improvement over previous iterations of ionization-based searches on AT-  
 984 LAS by providing additional background rejection with minimal loss in signal  
 985 efficiency.

986 The ionization measurement with the Pixel detector can be calibrated to pro-  
 987 vide an estimator of  $\beta\gamma$ . That estimate, together with the momentum measure-  
 988 ment provided by tracking, can be used to reconstruct a mass for each track  
 989 which traverses the pixel detector. That mass variable will be peaked at the [LLP](#)  
 990 mass for any signal, and provides an additional tool to search for an excess. In  
 991 addition to an explicit requirement on ionization, this search constructs a mass-  
 992 window for each targeted signal mass in order to evaluate any excess of events  
 993 and to set limits.

994 The strategy discussed here is optimized for lifetimes of  $O(1) - O(10)$  ns.  
 995 Pixel ionization is especially useful in this regime as particles only need to prop-  
 996 agate through the first seven layers of the inner detector, about 37 cm from the  
 997 beam axis. The search is still competitive with other searches for [LLPs](#) at longer  
 998 lifetimes, because the primary discriminating variables are still applicable even  
 999 for particles that do not decay within the detector [55]. Although the basic strat-  
 1000 egy remains the same for all lifetimes, two signal regions are defined to optimize  
 1001 separately for intermediate and long lifetime particles.

## 1002 11.1 TRIGGER

1003 Triggering remains a significant difficulty in defining an event selection with  
 1004 high signal efficiency in a search for [LLPs](#). There are no triggers available in  
 1005 the current ATLAS system that can fire directly from a high momentum track  
 1006 with large ionization (Section 6.6). Although in some configurations a charged  
 1007 [LLP](#) can fire muon triggers, this requirement introduces significant model depen-  
 1008 dence on both the allowed lifetimes and the interactions in the calorimeter [48].

1009 For a search targeting particles which may decay prior to reaching the muon  
 1010 system, the most efficient available trigger is based on missing energy [48]. As  
 1011 discussed in Section 10.1, signal events can produce  $E_T^{\text{miss}}$  by two primary mech-  
 1012 anisms. The decays of R-Hadrons to neutralinos can produce missing energy  
 1013 when the neutralinos go undetected in the calorimeters. [LLPs](#) which do not de-  
 1014 cay before the calorimeters also can produce missing energy because they do not  
 1015 deposit much energy. Either case to some extent relies on kinematic degrees of  
 1016 freedom to produce missing energy, as the pair-produced [LLPs](#) tend to balance  
 1017 each other in the transverse plain. That balance results in a relatively low ef-  
 1018 ficiency for long-lifetime particles, roughly 40%, and efficiencies between 65%  
 1019 and 95% for shorter lifetimes depending on both the mass and the lifetime.

## 1020 11.2 KINEMATICS AND ISOLATION

1021 After the trigger requirement, each event is required to have a primary vertex  
 1022 reconstructed from at least two well-measured tracks in the inner detector, each  
 1023 with  $p_T > 400$  MeV. If more than one such vertex exists, the primary vertex  
 1024 is taken to be the one with the largest summed track momentum for all tracks  
 1025 associated to that vertex. The offline reconstructed  $E_T^{\text{miss}}$  is required to be above  
 1026 130 GeV to additionally reject [SM](#) backgrounds. The transverse missing energy  
 1027 is calculated using fully reconstructed and calibrated offline objects, as described  
 1028 in Section 7.5. In particular the  $E_T^{\text{miss}}$  definition in this selection uses jets recon-  
 1029 structed with the anti- $k_t$  algorithm with radius  $R = 0.4$  from clusters of energy  
 1030 in the calorimeter (Section 7.2) and with  $p_T > 20$  GeV, as well as reconstructed  
 1031 muons, electrons, and tracks not identified as another object type.

1032 The  $E_T^{\text{miss}}$  distributions are shown for data and a few simulated signals in Fig-  
 1033 ure 22, after the trigger requirement. The cut placed at 130 GeV is 95% effi-  
 1034 cient for metastable and 90% efficient for stable particles, because of the missing  
 1035 energy generating mechanisms discussed previously. The distribution of data  
 1036 in this figure and subsequent figures in this section can be interpreted as the  
 1037 distribution of backgrounds, as any signal contamination would be negligible if  
 1038 present at these early stages of the selection (prior to the final requirement on  
 1039 ionization). The background falls rapidly with missing energy, motivating the  
 1040 direct requirement on  $E_T^{\text{miss}}$  for the signal region. Although a tighter require-  
 1041 ment than the specified value of 130 GeV would seem to increase the search  
 1042 potential from these early distributions, other requirements are more optimal  
 1043 when taken as a whole. The specific values for each requirement in signal region  
 1044 were optimized considering the increase in discovery reach for tightening the

1045 requirement on each discriminating variable. **NOTE: Is it interesting to dis-**  
 1046 **cuss the signal region optimization process in detail? I could add another**  
 1047 **section on how the values were determined, although in truth it is at least**  
 1048 **partially historical precedence.**

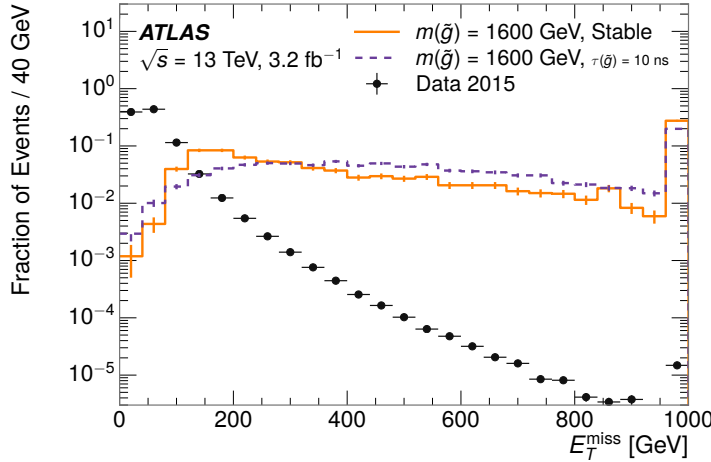


Figure 22: The distribution of  $E_T^{\text{miss}}$  for data and simulated signal events, after the trigger requirement.

1049 Potential signal events are then required to have at least one candidate LLP  
 1050 track. Although the LLPs are produced in pairs, many models do not consistently  
 1051 yield two charged particles. For example, in the R-Hadron model highlighted  
 1052 here, only 20% of events have two charged R-Hadrons while 47% of events have  
 1053 just one. A signal region requiring two charged candidates could be a powerful  
 1054 improvement in background rejection for a larger dataset, but it is not consid-  
 1055 ered in this version of the analysis as it was found to be unnecessary to reject the  
 1056 majority of backgrounds.

1057 For a track to be selected as a candidate, it must have  $p_T > 50 \text{ GeV}$  and pass  
 1058 basic quality requirements. The track must be associated to the primary vertex.  
 1059 It must also have at least seven clusters in the silicon layers in the inner detector  
 1060 to ensure an accurate measurement of momentum. Those clusters must include  
 1061 one in the innermost layer if the extrapolated track is expected to pass through  
 1062 that layer. And to ensure a reliable measurement of ionization, the track is re-  
 1063 quired to have at least two clusters in the pixel detector that provide a measure-  
 1064 ment of  $dE/dx$ .

1065 At this point in the selection, there is a significant high-ionization background  
 1066 from multiple tracks that significantly overlap in the inner detector. Previous  
 1067 version of this analysis have rejected these overlaps by an explicit overlap rejec-  
 1068 tion between pairs of fully reconstructed tracks, typically by requiring no addi-  
 1069 tional tracks within a cone around the candidate. This technique, however, fails  
 1070 to remove the background from tracks that overlap so precisely that the tracks  
 1071 cannot be separately resolved.

1072 A new method, added in Run 2, identifies cluster shapes that are likely formed  
 1073 by multiple tracks based on a neural network classification algorithm. The num-

1074   ber of clusters that are classified this way in the pixel detector for a given track  
 1075   is called  $N_{\text{split}}$ . As the shape of clusters requires significantly less spatial sepa-  
 1076   ration to identify overlaps than it does to reconstruct two fully resolved tracks,  
 1077   this variable is more effective at rejecting backgrounds from overlaps. Figure 23  
 1078   shows the dependence of ionization on  $N_{\text{split}}$ ; as  $N_{\text{split}}$  increases the most prob-  
 1079   able value of  $dE/dx$  grows significantly up to twice the expected value when  
 1080    $N_{\text{split}} = 4$ .

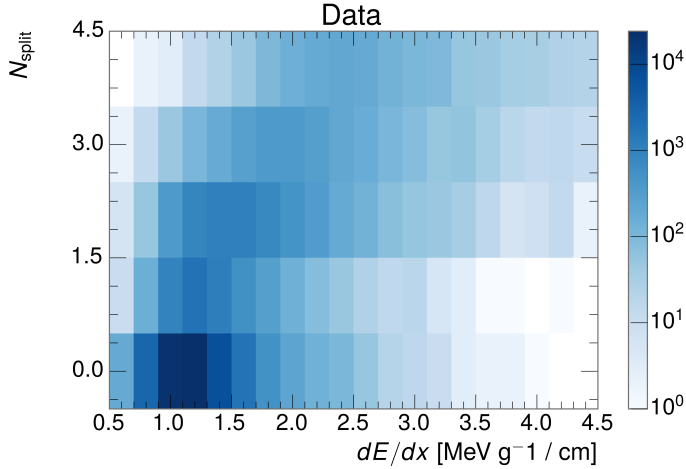


Figure 23: The dependence of  $dE/dx$  on  $N_{\text{split}}$  in data after basic track hit requirements have been applied.

1081   This requirement is very successful in reducing the long positive tail of the  
 1082    $dE/dx$  distributions, as can be seen in Figure 24. Comparing the distribution for  
 1083   “baseline tracks”, tracks with only the above requirements on clusters applied and  
 1084   before the requirement on  $N_{\text{split}}$ , to the distribution with  $N_{\text{split}} = 0$ , it is clear  
 1085   that the fraction of tracks with large  $dE/dx$  is reduced by several orders of mag-  
 1086   nitude. The isolated tracks are very close to the  $dE/dx$  distribution of identified  
 1087   muons, which are extremely well isolated on average. Figure 24 also includes  
 1088   the distribution of  $dE/dx$  in an example signal simulation to demonstrate how  
 1089   effective  $dE/dx$  is as a discriminating variable with this isolation applied. The  
 1090   background falls rapidly for  $dE/dx > 1.8 \text{ MeVg}^{-1}\text{cm}^2$  while the majority of  
 1091   the signal, approximately 90% depending on the mass, falls above that threshold.  
 1092   Over 90% of [LLP](#) tracks in simulated signal events pass the  $N_{\text{split}}$ -based isolation  
 1093   requirement.

1094   A few additional kinematic requirements are imposed to help reduce [SM](#) back-  
 1095   grounds. The momentum of the candidate track must be at least 150 GeV, and  
 1096   the uncertainty on that measurement must be less than 50%. The distribution of  
 1097   momentum is shown in Figure 25 for tracks in data and simulated signal events  
 1098   after the previously discussed requirements on clusters, transverse momentum,  
 1099   and isolation have been imposed. The signal particles are much harder on aver-

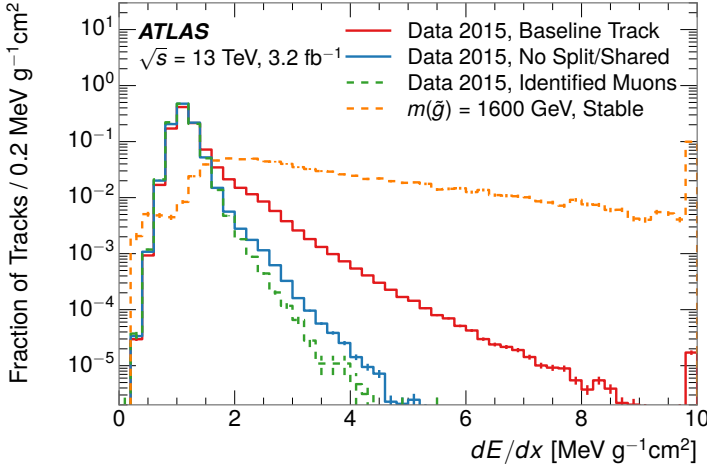


Figure 24: The distribution of  $dE/dx$  with various selections applied in data and simulated events.

age than their backgrounds because of the high energy interactions required to produce them. The transverse mass,  $M_T$ , defined as

$$M_T = \sqrt{2p_T E_T^{\text{miss}} (1 - \cos(\Delta\phi(E_T^{\text{miss}}, \text{track})))} \quad (1)$$

estimates the mass of a decay of to a single charged particle and an undetected particle and is required to be greater than 130 GeV to reject contributions from the decay of W bosons. Figure 26 shows the distribution of  $M_T$  for data and simulated signal events. The signal is distributed over a wide range of  $M_T$ , with about 90% above the threshold value of 130 GeV. The data shows a dual-peaked structure, where the first peak comes from W boson decays and the second peak is a kinematic shaping from the requirements on  $E_T^{\text{miss}}$  and the track  $p_T$  in dijet events.

### 11.3 STANDARD MODEL REJECTION

Because this search selects events with just a single, highly-ionizing track, backgrounds can be formed by a wide variety of SM processes when various charged particles have a few randomly large deposits of energy in the pixel detector. Those backgrounds can be effectively rejected by targeting the types of particles produced rather than the processes which produce them, as LLPs will have significant differences compared to any SM particle. These rejections focus on using additional features of the event, other than the kinematics or ionization of the candidate track, as they can provide a powerful source of background rejection with very high signal efficiency. The lifetime of the particle can significantly change its detector characteristics, as discussed in Section 10.1. To accommodate these differences, the SM rejections defined in this section are split to form two signal regions, one for long-lifetimes particles, the stable region, and one for intermediate lifetime particles, the metastable region.

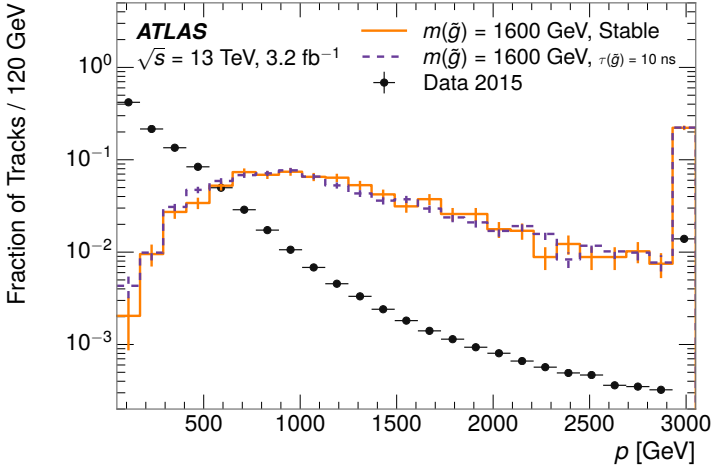


Figure 25: The distribution of track momentum for data and simulated signal events, after previous selection requirements have been applied.

1124 Jets can be very effectively rejected by considering the larger-scale isolation of  
 1125 the candidate track. In this case the isolation focuses on the production of nearby  
 1126 particles as a jet-veto, rather than isolation from overlapping tracks to reduce  
 1127 high-ionization backgrounds. As explained in Section 10.1, the fragmentation  
 1128 process which produces an R-Hadron is very hard and thus is not expected to  
 1129 produce additional particles. The jet-veto uses the summed momentum of tracks  
 1130 with a cone of  $\Delta R < 0.25$ , referred to as  $p_T^{\text{Cone}}$ , which is shown in Figure 27 for  
 1131 data and simulated signal events. In the data this value has a peak at zero from  
 1132 isolated tracks such as leptons, and a long tail from jets which contains as much  
 1133 as 80% of the background above 20 GeV at this stage of the selection. In signal  
 1134 events  $p_T^{\text{Cone}}$  is strongly peaked at zero and significantly less than 1% is above 20  
 1135 GeV. This makes a requirement of  $p_T^{\text{Cone}} < 20$  GeV one of the most effective  
 1136 methods to reject background without losing signal efficiency. For the stable  
 1137 signal region, this cut is further tightened to  $p_T^{\text{Cone}} < 5$  GeV as it is the most  
 1138 effective variable remaining to extend the search reach for long lifetimes.

1139 Even for fully isolated particles, there are additional methods to reject each  
 1140 type of particle using information in the muon system and calorimeters. Muons  
 1141 can be identified very reliably using the tracks in the muon system, as described  
 1142 in Section 7.4. For intermediate lifetimes the LLPs do not survive long enough  
 1143 to reach the muon system, and so muons are vetoed by rejecting tracks that as-  
 1144 sociate to a muon with medium muon identification requirements. For longer  
 1145 lifetimes, this rejection is not applied because LLPs which reach the muon system  
 1146 can be identified as muons as often as 30% of the time in simulated samples.

1147 Calorimeter-based particle rejection relies on the expected small deposits of  
 1148 energy from LLPs. When the lifetime is long enough to reach the calorimeter, a  
 1149 LLP deposits little of its energy as it traverses the material, as discussed in Sec-  
 1150 tion 10.1. Even when the particle does decay before the calorimeter, the major-  
 1151 ity of its energy is carried away by the LSP and not deposited in the calorimeter.  
 1152 In both cases the energy is expected to be distributed across the layers of the

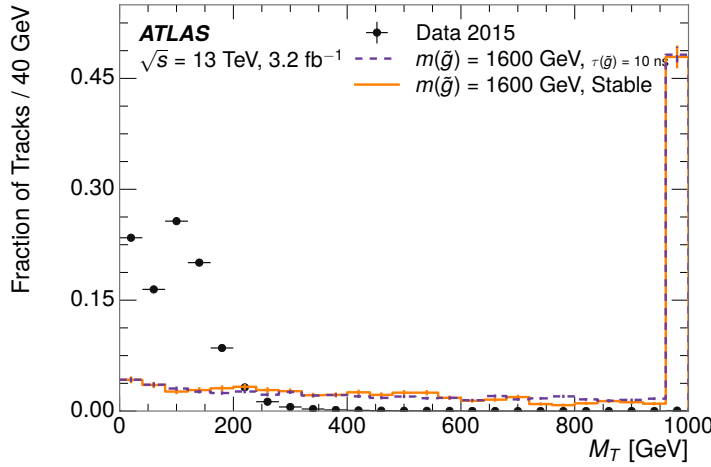


Figure 26: The distribution of  $M_T$  for data and simulated signal events, after previous selection requirements have been applied.

1153 calorimeters and not peaked in just one layer. This can be quantified in terms  
 1154 of  $E/p$ , the ratio of calorimeter energy of a nearby jet to the track momentum,  
 1155 and  $f_{EM}$ , the fraction of energy in that jet within the electromagnetic calorimeter.  
 1156 When no jets fall within a cone of 0.05 of the particle,  $E/p$  and  $f_{EM}$  are both  
 1157 defined as zero.  $E/p$  is expected to be above 1.0 for typical SM particles because  
 1158 of calibration and the contributions from other nearby particles. At these mo-  
 1159 ments there is no significant zero fraction due to interactions with the detector  
 1160 or insufficient energy deposits (see Section 8.2.2).  $f_{EM}$  is peaked close to 1.0 for  
 1161 electrons, and distributed between 10% and 90% for hadrons.

1162 These trends can be seen in the two dimensional distribution for signal in  
 1163 Figure 28 for stable and metastable (10 ns) events. The majority of R-Hadrons  
 1164 in both samples fall into the bin for  $E/p = 0$  and  $f_{EM} = 0$  because the majority  
 1165 of the time there is no associated jet. In the stable sample, when there often is  
 1166 an associated jet,  $E/p$  is typically still below 0.1, and the  $f_{EM}$  is predominantly  
 1167 under 0.8. In the metastable sample, on the other hand,  $E/p$  is larger but still  
 1168 typically below 0.1 because of actual jets produced during the decay. The  $f_{EM}$  is  
 1169 much lower on average in this case, below 0.1, because the 10 ns lifetime particles  
 1170 rarely decay before passing through the electromagnetic calorimeter. Figure 28  
 1171 also includes simulated Z decays to electrons or tau leptons. From the decays  
 1172 to electrons it is clear that the majority of electrons have  $f_{EM}$  above 0.9. The  
 1173 tau decays include a variety of products. Muons can be seen in the bin where  
 1174  $E/p = 0$  and  $f_{EM} = 0$  because they do not have an associated jet. Electrons fall  
 1175 into the range where  $E/p > 1$  and  $f_{EM} > 0.9$ . Hadronic tau decays are the most  
 1176 common, and fall in the range of  $0.1 < f_{EM} < 0.9$  and  $E/p > 1.0$ .

1177 These differences motivate an electron rejection by requiring an  $f_{EM}$  below  
 1178 0.9. Similarly, isolated hadrons are rejected by requiring  $E/p < 1.0$ . These re-  
 1179 quirements combine to remove the majority of isolated electrons and hadrons  
 1180 but retain over 95% of the simulated signal across a range of masses and lifetimes.

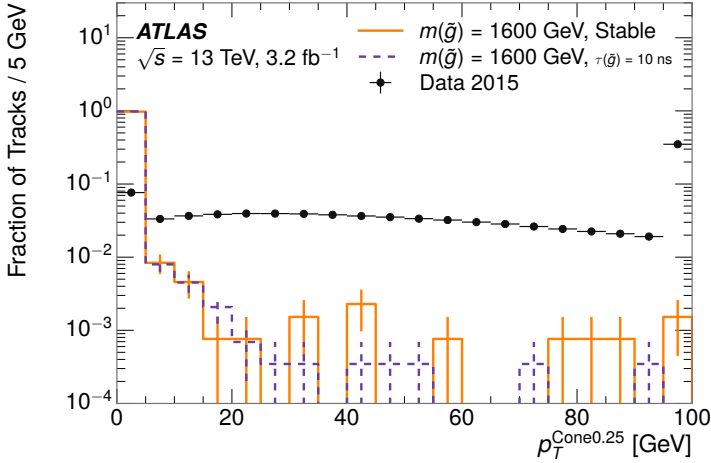


Figure 27: The distribution of summed tracked momentum within a cone of  $\Delta R < 0.25$  around the candidate track for data and simulated signal events, after previous selection requirements have been applied.

## 1181 11.4 IONIZATION

1182 The final requirements on the candidate track are the primary discriminating  
 1183 variables, the ionization in the pixel detector and the corresponding mass. That  
 1184 ionization is measured in terms of  $dE/dx$ , which was shown for data and sim-  
 1185 ulated signal events in Figure 24.  $dE/dx$  is dramatically greater for the high  
 1186 mass signal particles than the backgrounds, which start to fall immediately af-  
 1187 ter the minimally ionizing peak at  $1.1 \text{ MeV g}^{-1} \text{ cm}^2$ . The  $dE/dx$  for candidate  
 1188 tracks must be greater than a pseudorapidity-dependent threshold, specifically  
 1189  $1.80 - 0.11|\eta| + 0.17\eta^2 - 0.05\eta^3 \text{ MeV g}^{-1} \text{ cm}^{-2}$ , in order to correct for an ap-  
 1190 proximately 5% dependence of the MIP peak on  $\eta$ . The requirement was chosen  
 1191 as part of the signal region optimization, and manages to reduce the backgrounds  
 1192 by a factor of 100 while remaining 70-90% efficient for simulated signal events  
 1193 depending on the mass.

### 1194 11.4.1 MASS ESTIMATION

1195 The mean value of ionization in silicon is governed by the Bethe equation and  
 1196 the most probable value follows a Landau-Vavilov distribution [49]. Those forms  
 1197 inspire a parametric description of  $dE/dx$  in terms of  $\beta\gamma$ ,

$$(dE/dx)_{\text{MPV}}(\beta\gamma) = \frac{p_1}{\beta p_3} \ln(1 + [p_2 \beta\gamma]^{p_5}) - p_4 \quad (2)$$

1198 which performs well in the range  $0.3 < \beta\gamma < 1.5$ . This range includes the ex-  
 1199 pected range of  $\beta\gamma$  for the particles targeted for this search, with  $\beta\gamma \approx 2.0$  for  
 1200 lower mass particles ( $O(100 \text{ GeV})$ ) and up to  $\beta\gamma \approx 0.5$  for higher mass par-  
 1201 ticles ( $O(1000 \text{ GeV})$ ). The parameters,  $p_i$ , are fit using a 2015 data sample of

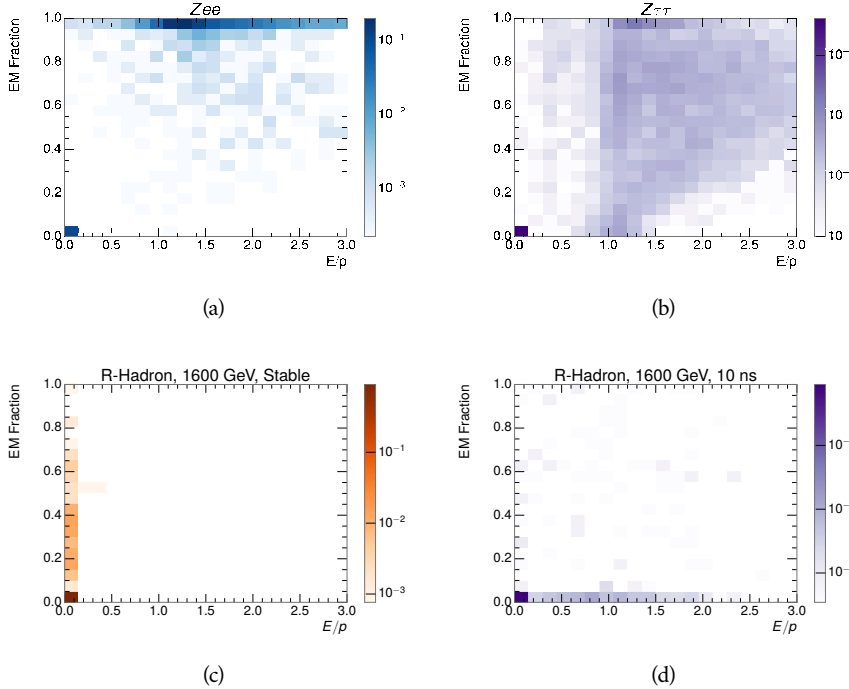


Figure 28: The normalized, two-dimensional distribution of  $E/p$  and  $f_{EM}$  for simulated  
 (a)  $Z \rightarrow ee$ , (b)  $Z \rightarrow \tau\tau$ , (c) 1200 GeV Stable R-Hadron events, and (d) 1200  
 GeV, 10 ns R-Hadron events.

1202 low-momentum pions, kaons, and protons as described in Ref. [56]. Figure 29  
 1203 shows the two-dimensional distribution of  $dE/dx$  and momentum along with  
 1204 the above fitted values for  $(dE/dx)_{MPV}$ .

1205 The above equation (2) is then numerically inverted to estimate  $\beta\gamma$  and the  
 1206 mass for each candidate track. In simulated signal events, the mean of this mass  
 1207 value reproduces the generated mass up to around 1800 GeV to within 3%, and  
 1208 3% shift is applied to correct for this difference. The mass distributions prior to  
 1209 this correction are shown for a few stable mass points in Figure 30. The large  
 1210 widths of these distributions come from the high variability in energy deposits  
 1211 in the pixel detector, but the means converge to the expected values.

1212 This analysis evaluates expected yields and the resulting cross sectional lim-  
 1213 its using windows in this mass variable. The windows are formed by fitting  
 1214 mass distributions like those in Figure 30 to Gaussian distributions and taking  
 1215 all events that fall within  $\pm 1.4\sigma$  of the mean. As can be seen in Figure 30, typical  
 1216 values for this width are  $\sigma \approx 300 - 500$  GeV depending on the generated mass.

## 1217 11.5 EFFICIENCY

1218 The numbers of events passing each requirement through ionization are shown  
 1219 in Table 2 for the full 2015 dataset and a simulated 1600 GeV, 10 ns lifetime R-  
 1220 Hadron sample. The table highlights the overall acceptance  $\times$  efficiency for sig-  
 1221 nificant events, which for this example is 19%. Between SM rejection and ionization,

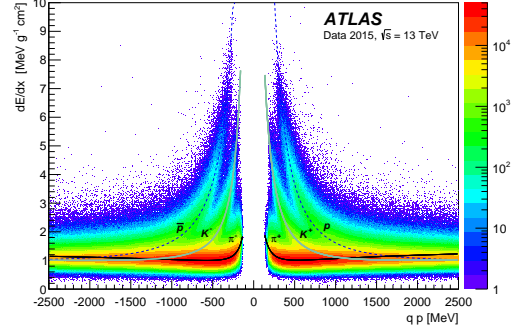


Figure 29: Two-dimensional distribution of  $dE/dx$  versus charge signed momentum ( $qp$ ) for minimum-bias tracks. The fitted distributions of the most probable values for pions, kaons and protons are superimposed.

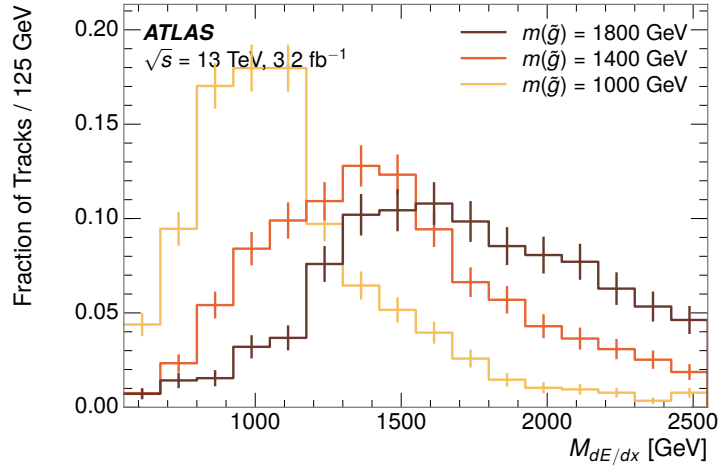


Figure 30: The distribution of mass estimated using  $dE/dx$  for simulated stable R-Hadrons with masses between 1000 and 1600 GeV.

1222 this signal region reduces the background of tracks which pass the kinematic  
 1223 requirements down by an additional factor of almost 2000.

Selection	Exp. Signal Events	Observed Events in $3.2 \text{ fb}^{-1}$
Generated	$26.0 \pm 0.3$	
$E_T^{\text{miss}}$ Trigger	$24.8 \pm 0.3$ (95%)	
$E_T^{\text{miss}} > 130 \text{ GeV}$	$23.9 \pm 0.3$ (92%)	
Track Quality and $p_T > 50$	$10.7 \pm 0.2$ (41%)	368324
Isolation Requirement	$9.0 \pm 0.2$ (35%)	108079
Track $p > 150 \text{ GeV}$	$6.6 \pm 0.2$ (25%)	47463
$M_T > 130 \text{ GeV}$	$5.8 \pm 0.2$ (22%)	18746
Electron and Hadron Veto	$5.5 \pm 0.2$ (21%)	3612
Muon Veto	$5.5 \pm 0.2$ (21%)	1668
Ionization Requirement	$5.0 \pm 0.1$ (19%)	11

Table 2: The expected number of events at each level of the selection for metastable  $1600 \text{ GeV}$ ,  $10 \text{ ns}$  R-Hadrons, along with the number of events observed in data, for  $3.2 \text{ fb}^{-1}$ . The simulated yields are shown with statistical uncertainties only. The total efficiency  $\times$  acceptance is also shown for the signal.

1224 There is a strong dependence of this efficiency on lifetime and mass, with effi-  
 1225 ciencies dropping to under 1% at low lifetimes. Figure 31 shows the dependence  
 1226 on both mass and lifetime for all signal samples considered in this search. The  
 1227 dependence on mass is relatively slight and comes predominantly from the in-  
 1228 creasing fraction of R-Hadrons which pass the ionization cut with increasing  
 1229 mass. The trigger and  $E_T^{\text{miss}}$  requirements are most efficient for particles that  
 1230 decay before reaching the calorimeters. However, the chance of a particle to be  
 1231 reconstructed as a high-quality track decreases significantly at low lifetimes as  
 1232 the particle does not propagate sufficiently through the inner detector. These  
 1233 effects lead to a maximum in the selection efficiency for lifetimes around 10-30  
 1234 ns.

1235 The inefficiency of this signal region at short lifetimes comes almost exclu-  
 1236 sively from an acceptance effect, in that the particles do not reach the necessary  
 1237 layers of the SCT. This can be seen more clearly by defining a fiducial region  
 1238 which includes events with at least one R-Hadron that is produced with non-  
 1239 zero charge,  $p_T > 50 \text{ GeV}$ ,  $p > 150 \text{ GeV}$ ,  $|\eta| < 2.5$ , and a decay distance greater  
 1240 than 37 cm in the transverse plane. At short (1 ns) lifetimes, the acceptance into  
 1241 this region is as low as 4%. Once this acceptance is accounted for, the selection  
 1242 efficiency ranges from 25% at lifetimes of 1 ns up to 45% at lifetimes of 10 ns.

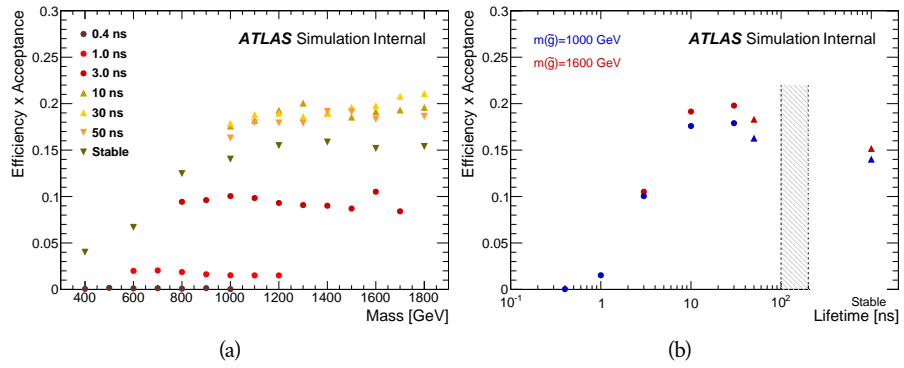


Figure 31: The acceptance  $\times$  efficiency as a function of R-Hadron (a) mass and (b) lifetime. (a) shows all of the combinations of mass and lifetime considered in this search, and (b) highlights the lifetime dependence for 1000 GeV and 1600 GeV R-Hadrons.

1243

1244 BACKGROUND ESTIMATION

---

1245 The event selection discussed in the previous section focuses on detector sig-  
 1246 natures, emphasizing a single high-momentum, highly-ionizing track. That track  
 1247 is then required to be in some way inconsistent with the expected properties  
 1248 of SM particles, with various requirements designed to reject jets, hadrons, elec-  
 1249 trons, and muons (Section 11.3). So the background for this search comes en-  
 1250 tirely from reducible backgrounds that are outliers of various distributions like  
 1251  $dE/dx$ ,  $f_{EM}$ , and  $p_T^{\text{Cone}}$ . The simulation can be tuned in various ways to do an  
 1252 excellent job of modeling the average properties of each particle type [57], but it  
 1253 is not necessarily expected to accurately reproduce outliers. For these reasons,  
 1254 the background estimation used for this search is estimated entirely using data.

## 1255 12.1 BACKGROUND SOURCES

1256 Charged particles with lifetimes long enough to form tracks in the inner detector  
 1257 can be grouped into three major categories based on their detector interactions:  
 1258 hadrons, electrons, and muons. Every particle that enters into the background  
 1259 for this search belongs to one of these types. Relatively pure samples of each of  
 1260 these types can be formed in data by inverting the various rejection techniques  
 1261 in Section 11.3. Specifically, muons are selected requiring medium muon identi-  
 1262 fication, electrons requiring  $E/p > 1.0$  and  $f_{EM} > 0.95$ , and hadrons requiring  
 1263  $E/p > 1.0$  and  $f_{EM} < 0.95$ .

1264 Figure 32 shows the distributions of momentum and  $dE/dx$  for these cate-  
 1265 gories in data, after requiring the event level selection as well as the track re-  
 1266 quirements on  $p_T$ , hits, and  $N_{\text{split}}$ , as discussed in Section 11.2. Simulated signal  
 1267 events are included for reference. These distribution are only illustrative of the  
 1268 differences between types, as the rejection requirements could alter their shape.  
 1269 This is especially significant for momentum which enters directly into  $E/p$  and  
 1270 can indirectly affect muon identification. However the various types show clear  
 1271 differences in both distributions. Momentum is expected to vary significantly  
 1272 because of the production mechanisms for the different species. **Note for Laura:**  
 1273 **Interesting that the momentum tail is so much higher for electrons than**  
 1274 **muons, any idea why that would happen?**  $dE/dx$  is different between types  
 1275 because of incomplete isolation; although the requirement on  $N_{\text{split}}$  helps to re-  
 1276 duce the contribution of nearby particles it does not completely remove the ef-  
 1277 fect of overlaps. Muons are better isolated and thus have the smallest fraction  
 1278 of  $dE/dx$  above the threshold of  $1.8 \text{ MeVg}^{-1}\text{cm}^2$ ; hadrons and electrons have  
 1279 a larger fraction above this threshold.

1280 It is difficult to determine what fraction of each particle type enters into the fi-  
 1281 nal signal region. The background method will not have significant dependence

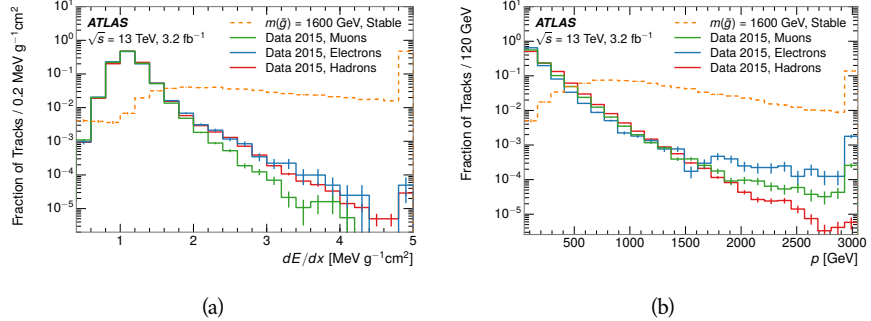


Figure 32: The distribution of (a)  $dE/dx$  and (b) momentum for tracks in data and simulated signal after requiring the event level selection and the track selection on  $p_T$ , hits, and  $N_{\text{split}}$ . Each sub-figure shows the normalized distributions for tracks classified as hadrons, electrons, and muons in data and R-Hadrons in the simulated signal.

on the relative contributions of each species, but it is useful to understand the differences between each when considering the various tests of the method.

## 12.2 PREDICTION METHOD

The data-driven background estimation relies on the independence of ionization and other aspects of the event. For standard model particles with momenta above 50 GeV,  $dE/dx$  is not correlated with momentum. So, the proposed method to estimate the mass distribution of the signal region is to use momentum from a track with low  $dE/dx$  (below the threshold value) and to combine it with a random  $dE/dx$  value from a  $dE/dx$  template. The resulting track is just as likely as the original, so a number of such random generations forms a distribution of mass for the signal region.

Algorithmically this method is implemented by forming two distinct Control Regions (CRs). The first CR, CR1, is formed by applying the entire event selection from Chapter 11 up to the  $dE/dx$  and mass requirements. The  $dE/dx$  requirement is instead inverted for this region. Because of the independence of  $dE/dx$ , the tracks in this control region have the same kinematic distribution as the tracks in the signal region, and are used to measure a two-dimensional template of  $p$  and  $\eta$ . The second CR, CR2, is formed from the event selection through the  $dE/dx$  requirement, but with an inverted  $E_T^{\text{miss}}$  requirement. The tracks in this control region are expected to have similar  $dE/dx$  distributions to the signal region, and so this region is used to measure a two-dimensional template of  $dE/dx$  and  $\eta$ .

The contribution of any signal to the control regions is minimized by the inverted selection requirements. Only less than 10% of simulated signal events have either  $dE/dx$  or  $E_T^{\text{miss}}$  below the threshold values in the original signal region, while the backgrounds are significantly enhanced by inverting those requirements. The signal contamination is less than 1% in both control regions for all of the simulated masses and lifetimes considered in this analysis.

With those measured templates, the shape of the mass estimation is generated by first selecting a random ( $p$ ,  $\eta$ ) combination from CR1. This momentum value is combined with a  $dE/dx$  value taken from the appropriate distribution of  $dE/dx$  for the selected  $\eta$  from CR2. The use of  $\eta$  in both random samplings controls for any correlation between  $p$ ,  $dE/dx$ , and  $\eta$ . Those values are then used to calculate a mass in the same way that is done for regular tracks in data, see Section 11.4.1. As this procedure includes all  $dE/dx$  values, the cut at 1.8 MeVg $^{-1}$ cm $^2$  is then enforced to fully model the signal region. The generated mass distribution is then normalized by scaling the background estimate to the data in the region  $M < 160$  GeV, where signals of this type have already been excluded [54]. This normalization takes place before the ionization requirement.

## 12.3 VALIDATION

The validity of the background estimation technique can be evaluated in both data and simulation. The underlying assumption that random combinations of  $dE/dx$  and momentum can predict a mass distribution in an orthogonal region can be tested using simulated samples where concerns like multiple particle types can be controlled. Using the same technique in another set of signal-depleted regions in data then extends this confidence to the more complicated case where several particle species are inherently included.

### 12.3.1 CLOSURE IN SIMULATION

The first test of the procedure is done using a simulated sample of  $W \rightarrow \mu\nu$  decays. These types of events provide the ingredients required to test the background estimate,  $E_T^{\text{miss}}$  and isolated tracks, with high statistics. In this example there is no signal, so simulated events in the orthogonal CRs are used to estimate the shape of the mass distribution of the simulated events in the signal region. To reflect the different topology for W boson decays, the CRs use slightly modified definitions. In all CRs, the requirement of  $p > 150$  GeV and the SM rejection requirements are removed. Additionally, for the signal region the requirement on  $E_T^{\text{miss}}$  is relaxed to 30 GeV and the corresponding inverted requirement on CR2 is also set at 30 GeV.

With these modified selections, the simulated and randomly generated distributions of  $M_{dE/dx}$  are shown in Figure 33. This figure includes the mass distributions before and after the requirement on  $dE/dx$ , which significantly shapes the distributions. In both cases the background estimation technique reproduces the shape of  $M_{dE/dx}$  in the signal region. There is a small difference in the positive tail of the mass distribution prior to the ionization cut, where the random events underestimate the fraction of tracks with mass above 150 GeV by about 20%. After the ionization requirement, however, this discrepancy is not present and the two distributions agree to within statistical uncertainties.

This ability to reproduce the shape of the mass distribution in simulated events shows that the technique works as expected. No significant biases are acquired in using low  $dE/dx$  events to select kinematic templates or in using low  $E_T^{\text{miss}}$

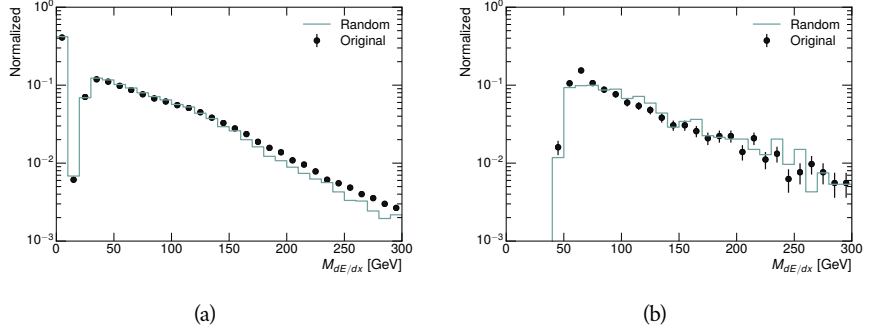


Figure 33: The distribution of  $M_{dE/dx}$  (a) before and (b) after the ionization requirement for tracks in simulated W boson decays and for the randomly generated background estimate.

1352 events to select ionization templates, as either would result in a mismodeling of  
 1353 the shape of the mass distribution. The simulated events contain only one par-  
 1354 ticle type, however, so this test only establishes that the technique works well  
 1355 when the the CRs are populated by exactly the same species.

### 1356 12.3.2 VALIDATION REGION IN DATA

1357 The second test of the background estimate is performed using data in an or-  
 1358 thogonal validation region. The validation region, and the corresponding CRs,  
 1359 are formed using the same selection requirements as in the nominal method but  
 1360 with a modified requirement on momentum,  $50 < p[\text{GeV}] < 150$ . This allows  
 1361 the technique to be checked in a region with very similar properties but where  
 1362 the signal is depleted, as the majority of the signal has momentum above 150  
 1363 GeV while the backgrounds are enhanced below that threshold. Any biases on  
 1364 the particle composition of the CRs for the signal region will be reflected in the  
 1365 CRs used to estimate the mass distribution in the validation region.

1366 Figure 34 shows the measured and randomly generated mass distributions for  
 1367 data before and after the ionization requirement. The background estimate does  
 1368 an excellent job of modeling the actual background before the ionization require-  
 1369 ment, with good agreement to within the statistical uncertainties out to the limit  
 1370 of the mass distribution. There are very few events in the validation region after  
 1371 the ionization requirement, but the few observed events are consistent with the  
 1372 background prediction. The good agreement in this validation region provides  
 1373 a confirmation that the technique works even in the full-complexity case with  
 1374 multiple particle types entering the distributions. Any bias from changes in par-  
 1375 ticle composition between regions is small compared to statistical uncertainties.

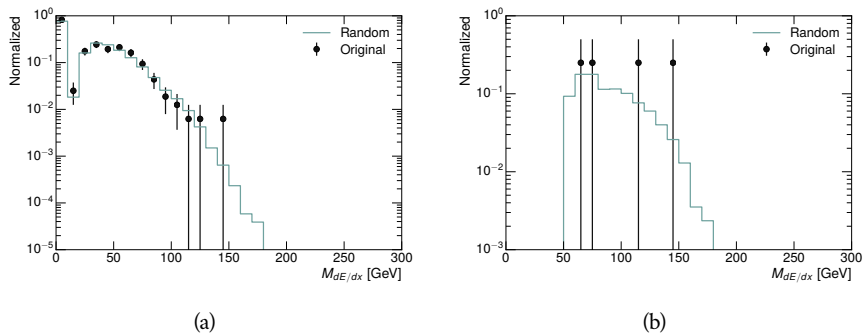


Figure 34: The distribution of  $M_{dE/dx}$  (a) before and (b) after the ionization requirement for tracks in the validation region and for the randomly generated background estimate.



# 13

1376

## 1377 SYSTEMATIC UNCERTAINTIES AND RESULTS

---

### 1378 13.1 SYSTEMATIC UNCERTAINTIES

### 1379 13.2 FINAL YIELDS



# 14

1380

## 1381 INTERPRETATION

---

1382 14.1 CROSS SECTIONAL LIMITS

1383 14.2 MASS LIMITS

1384 14.3 CONTEXT FOR LONG-LIVED SEARCHES



1385

## PART VI

1386

## CONCLUSIONS

1387

You can put some informational part preamble text here.



# 15

1388

1389 SUMMARY AND OUTLOOK

---

1390 15.1 SUMMARY

1391 15.2 OUTLOOK



1392

## PART VII

1393

## APPENDIX

1394



# A

1395

1396 INELASTIC CROSS SECTION

---



# B

1397

## 1398 APPENDIX TEST

---

1399 Examples: *Italics*, SMALL CAPS, ALL CAPS <sup>1</sup>. Acronym testing: **UML!** (**UML!**) –  
1400 **UML! – UML! (UML!) – UML!s**

This appendix is temporary and is here to be used to check the style of the document.

### 1401 B.1 APPENDIX SECTION TEST

1402 Random text that should take up a few lines. The purpose is to see how sections  
1403 and subsections flow with some actual context. Without some body copy be-  
1404 tween each heading it can be difficult to tell if the weight of the fonts, styles, and  
1405 sizes use work well together.

#### 1406 B.1.1 APPENDIX SUBECTION TEST

1407 Random text that should take up a few lines. The purpose is to see how sections  
1408 and subsections flow with some actual context. Without some body copy be-  
1409 tween each heading it can be difficult to tell if the weight of the fonts, styles, and  
1410 sizes use work well together.

### 1411 B.2 A TABLE AND LISTING

1412 Curabitur tellus magna, porttitor a, commodo a, commodo in, tortor. Donec in-  
1413 terdum. Praesent scelerisque. Maecenas posuere sodales odio. Vivamus metus  
1414 lacus, varius quis, imperdiet quis, rhoncus a, turpis. Etiam ligula arcu, elemen-  
1415 tum a, venenatis quis, sollicitudin sed, metus. Donec nunc pede, tincidunt in,  
1416 venenatis vitae, faucibus vel, nibh. Pellentesque wisi. Nullam malesuada. Morbi  
1417 ut tellus ut pede tincidunt porta. Lorem ipsum dolor sit amet, consectetur adip-  
1418 iscing elit. Etiam congue neque id dolor.

1419 There is also a Python listing below Listing 1.

---

1 Footnote example.

LABITUR BONORUM PRI NO	QUE VISTA	HUMAN
fastidii ea ius	germano	demonstratea
suscipit instructior	titulo	personas
quaestio philosophia	facto	demonstrated

Table 3: Autem usu id.

## 1420 B.3 SOME FORMULAS

Due to the statistical nature of ionisation energy loss, large fluctuations can occur in the amount of energy deposited by a particle traversing an absorber element<sup>2</sup>. Continuous processes such as multiple scattering and energy loss play a relevant role in the longitudinal and lateral development of electromagnetic and hadronic showers, and in the case of sampling calorimeters the measured resolution can be significantly affected by such fluctuations in their active layers. The description of ionisation fluctuations is characterised by the significance parameter  $\kappa$ , which is proportional to the ratio of mean energy loss to the maximum allowed energy transfer in a single collision with an atomic electron:

*You might get unexpected results using math in chapter or section heads. Consider the pdfspacing option.*

$$\kappa = \frac{\xi}{E_{\max}} \quad (3)$$

$E_{\max}$  is the maximum transferable energy in a single collision with an atomic electron.

$$E_{\max} = \frac{2m_e\beta^2\gamma^2}{1 + 2\gamma m_e/m_x + (m_e/m_x)^2},$$

1421 where  $\gamma = E/m_x$ ,  $E$  is energy and  $m_x$  the mass of the incident particle,  $\beta^2 = 1 - 1/\gamma^2$  and  $m_e$  is the electron mass.  $\xi$  comes from the Rutherford scattering cross section and is defined as:

$$\xi = \frac{2\pi z^2 e^4 N_{Av} Z \rho \delta x}{m_e \beta^2 c^2 A} = 153.4 \frac{z^2}{\beta^2} \frac{Z}{A} \rho \delta x \text{ keV},$$

1424 where

- z charge of the incident particle
- $N_{Av}$  Avogadro's number
- Z atomic number of the material
- A atomic weight of the material
- $\rho$  density
- $\delta x$  thickness of the material
- 1426  $\kappa$  measures the contribution of the collisions with energy transfer close to  $E_{\max}$ . For a given absorber,  $\kappa$  tends towards large values if  $\delta x$  is large and/or if 1427  $\beta$  is small. Likewise,  $\kappa$  tends towards zero if  $\delta x$  is small and/or if  $\beta$  approaches 1428 1.
- 1429

2 Examples taken from Walter Schmidt's great gallery:  
<http://home.vrweb.de/~was/mathfonts.html>

Listing 1: A floating example (listings manual)

---

```
1 for i in xrange(10):
    print i, i*i, i*i*i
print "done"
```

---

1430        The value of  $\kappa$  distinguishes two regimes which occur in the description of  
1431        ionisation fluctuations:

- 1432        1. A large number of collisions involving the loss of all or most of the incident  
1433        particle energy during the traversal of an absorber.

1434        As the total energy transfer is composed of a multitude of small energy  
1435        losses, we can apply the central limit theorem and describe the fluctua-  
1436        tions by a Gaussian distribution. This case is applicable to non-relativistic  
1437        particles and is described by the inequality  $\kappa > 10$  (i. e., when the mean en-  
1438        ergy loss in the absorber is greater than the maximum energy transfer in  
1439        a single collision).

- 1440        2. Particles traversing thin counters and incident electrons under any condi-  
1441        tions.

1442        The relevant inequalities and distributions are  $0.01 < \kappa < 10$ , Vavilov  
1443        distribution, and  $\kappa < 0.01$ , Landau distribution.



- 1445 [1] S. Agostinelli et al. “GEANT4: A simulation toolkit”. In: *Nucl. Instrum. Meth.*  
1446 A 506 (2003), pp. 250–303. doi: [10.1016/S0168-9002\(03\)01368-8](https://doi.org/10.1016/S0168-9002(03)01368-8).
- 1447 [2] ATLAS Collaboration. “A study of the material in the ATLAS inner de-  
1448 tector using secondary hadronic interactions”. In: *JINST* 7 (2012), P01013.  
1449 doi: [10.1088/1748-0221/7/01/P01013](https://doi.org/10.1088/1748-0221/7/01/P01013). arXiv: [1110.6191 \[hep-ex\]](https://arxiv.org/abs/1110.6191).  
1450 [PERF-2011-08](#).
- 1451 [3] ATLAS Collaboration. “Electron and photon energy calibration with the  
1452 ATLAS detector using LHC Run 1 data”. In: *Eur. Phys. J. C* 74 (2014), p. 3071.  
1453 doi: [10.1140/epjc/s10052-014-3071-4](https://doi.org/10.1140/epjc/s10052-014-3071-4). arXiv: [1407.5063](https://arxiv.org/abs/1407.5063)  
1454 [hep-ex]. [PERF-2013-05](#).
- 1455 [4] ATLAS Collaboration. “A measurement of the calorimeter response to sin-  
1456 ggle hadrons and determination of the jet energy scale uncertainty using  
1457 LHC Run-1  $pp$ -collision data with the ATLAS detector”. In: (2016). arXiv:  
1458 [1607.08842 \[hep-ex\]](https://arxiv.org/abs/1607.08842). [PERF-2015-05](#).
- 1459 [5] ATLAS Collaboration. “Single hadron response measurement and calorime-  
1460 ter jet energy scale uncertainty with the ATLAS detector at the LHC”. In:  
1461 *Eur. Phys. J. C* 73 (2013), p. 2305. doi: [10.1140/epjc/s10052-013-2305-1](https://doi.org/10.1140/epjc/s10052-013-2305-1). arXiv: [1203.1302 \[hep-ex\]](https://arxiv.org/abs/1203.1302). [PERF-2011-05](#).
- 1463 [6] ATLAS Collaboration. “The ATLAS Simulation Infrastructure”. In: *Eur.*  
1464 *Phys. J. C* 70 (2010), p. 823. doi: [10.1140/epjc/s10052-010-1429-9](https://doi.org/10.1140/epjc/s10052-010-1429-9).  
1465 arXiv: [1005.4568 \[hep-ex\]](https://arxiv.org/abs/1005.4568). [SOFT-2010-01](#).
- 1466 [7] T. Sjöstrand, S. Mrenna, and P. Skands. “A Brief Introduction to PYTHIA  
1467 8.1”. In: *Comput. Phys. Commun.* 178 (2008), pp. 852–867. doi: [10.1016/j.cpc.2008.01.036](https://doi.org/10.1016/j.cpc.2008.01.036). arXiv: [0710.3820](https://arxiv.org/abs/0710.3820).
- 1469 [8] ATLAS Collaboration. *Summary of ATLAS Pythia 8 tunes*. ATL-PHYS-PUB-  
1470 2012-003. 2012. URL: <http://cds.cern.ch/record/1474107>.
- 1471 [9] A.D. Martin, W.J. Stirling, R.S. Thorne, and G. Watt. “Parton distributions  
1472 for the LHC”. In: *Eur. Phys. J. C* 63 (2009). Figures from the [MSTW Website](#),  
1473 pp. 189–285. doi: [10.1140/epjc/s10052-009-1072-5](https://doi.org/10.1140/epjc/s10052-009-1072-5). arXiv: [0901.0002](https://arxiv.org/abs/0901.0002).
- 1475 [10] A. Sherstnev and R.S. Thorne. “Parton Distributions for LO Generators”.  
1476 In: *Eur. Phys. J. C* 55 (2008), pp. 553–575. doi: [10.1140/epjc/s10052-008-0610-x](https://doi.org/10.1140/epjc/s10052-008-0610-x). arXiv: [0711.2473](https://arxiv.org/abs/0711.2473).
- 1478 [11] A. Ribon et al. *Status of Geant4 hadronic physics for the simulation of LHC*  
1479 *experiments at the start of LHC physics program*. CERN-LCGAPP-2010-02.  
1480 2010. URL: <http://lcgapp.cern.ch/project/docs/noteStatusHadronic2010.pdf>.

- 1482 [12] M. P. Guthrie, R. G. Alsmiller, and H. W. Bertini. "Calculation of the cap-  
 1483 ture of negative pions in light elements and comparison with experiments  
 1484 pertaining to cancer radiotherapy". In: *Nucl. Instrum. Meth.* 66 (1968), pp. 29–  
 1485 36. doi: [10.1016/0029-554X\(68\)90054-2](https://doi.org/10.1016/0029-554X(68)90054-2).
- 1486 [13] H. W. Bertini and P. Guthrie. "News item results from medium-energy  
 1487 intranuclear-cascade calculation". In: *Nucl. Instr. and Meth. A* 169 (1971),  
 1488 p. 670. doi: [10.1016/0375-9474\(71\)90710-X](https://doi.org/10.1016/0375-9474(71)90710-X).
- 1489 [14] V.A. Karmanov. "Light Front Wave Function of Relativistic Composite  
 1490 System in Explicitly Solvable Model". In: *Nucl. Phys. B* 166 (1980), p. 378.  
 1491 doi: [10.1016/0550-3213\(80\)90204-7](https://doi.org/10.1016/0550-3213(80)90204-7).
- 1492 [15] H. S. Fesefeldt. *GHEISHA program*. Pitha-85-02, Aachen. 1985.
- 1493 [16] G. Folger and J.P. Wellisch. "String parton models in Geant4". In: (2003).  
 1494 arXiv: [nucl-th/0306007](https://arxiv.org/abs/nucl-th/0306007).
- 1495 [17] N. S. Amelin et al. "Transverse flow and collectivity in ultrarelativistic  
 1496 heavy-ion collisions". In: *Phys. Rev. Lett.* 67 (1991), p. 1523. doi: [10.1103/PhysRevLett.67.1523](https://doi.org/10.1103/PhysRevLett.67.1523).
- 1498 [18] N. S. Amelin et al. "Collectivity in ultrarelativistic heavy ion collisions". In:  
 1499 *Nucl. Phys. A* 544 (1992), p. 463. doi: [10.1016/0375-9474\(92\)90598-E](https://doi.org/10.1016/0375-9474(92)90598-E).
- 1501 [19] L. V. Bravina et al. "Fluid dynamics and Quark Gluon string model - What  
 1502 we can expect for Au+Au collisions at 11.6 AGeV/c". In: *Nucl. Phys. A* 566  
 1503 (1994), p. 461. doi: [10.1016/0375-9474\(94\)90669-6](https://doi.org/10.1016/0375-9474(94)90669-6).
- 1504 [20] L. V. Bravin et al. "Scaling violation of transverse flow in heavy ion colli-  
 1505 sions at AGS energies". In: *Phys. Lett. B* 344 (1995), p. 49. doi: [10.1016/0370-2693\(94\)01560-Y](https://doi.org/10.1016/0370-2693(94)01560-Y).
- 1507 [21] B. Andersson et al. "A model for low-pT hadronic reactions with general-  
 1508 izations to hadron-nucleus and nucleus-nucleus collisions". In: *Nucl. Phys.*  
 1509 *B* 281 (1987), p. 289. doi: [10.1016/0550-3213\(87\)90257-4](https://doi.org/10.1016/0550-3213(87)90257-4).
- 1510 [22] B. Andersson, A. Tai, and B.-H. Sa. "Final state interactions in the (nuclear)  
 1511 FRITIOF string interaction scenario". In: *Z. Phys. C* 70 (1996), pp. 499–  
 1512 506. doi: [10.1007/s002880050127](https://doi.org/10.1007/s002880050127).
- 1513 [23] B. Nilsson-Almqvist and E. Stenlund. "Interactions Between Hadrons and  
 1514 Nuclei: The Lund Monte Carlo, Fritiof Version 1.6". In: *Comput. Phys. Com-*  
 1515 *mun.* 43 (1987), p. 387. doi: [10.1016/0010-4655\(87\)90056-7](https://doi.org/10.1016/0010-4655(87)90056-7).
- 1516 [24] B. Ganhuyag and V. Uzhinsky. "Modified FRITIOF code: Negative charged  
 1517 particle production in high energy nucleus nucleus interactions". In: *Czech.*  
 1518 *J. Phys.* 47 (1997), pp. 913–918. doi: [10.1023/A:1021296114786](https://doi.org/10.1023/A:1021296114786).
- 1519 [25] ATLAS Collaboration. "Topological cell clustering in the ATLAS calorime-  
 1520 ters and its performance in LHC Run 1". In: (2016). arXiv: [1603.02934](https://arxiv.org/abs/1603.02934)  
 1521 [[hep-ex](#)].
- 1522 [26] Peter Speckmayer. "Energy Measurement of Hadrons with the CERN AT-  
 1523 LAS Calorimeter". Presented on 18 Jun 2008. PhD thesis. Vienna: Vienna,  
 1524 Tech. U., 2008. URL: <http://cds.cern.ch/record/1112036>.

- 1525 [27] CMS Collaboration. “The CMS barrel calorimeter response to particle  
 1526 beams from 2 to 350 GeV/c”. In: *Eur. Phys. J. C* 60.3 (2009). doi: [10.1140/epjc/s10052-009-0959-5](https://doi.org/10.1140/epjc/s10052-009-0959-5).
- 1528 [28] J. Beringer et al. (Particle Data Group). “Review of Particle Physics”. In:  
 1529 *Chin. Phys. C* 38 (2014), p. 090001. URL: <http://pdg.lbl.gov>.
- 1530 [29] P. Adragna et al. “Measurement of Pion and Proton Response and Lon-  
 1531 gitudinal Shower Profiles up to 20 Nuclear Interaction Lengths with the  
 1532 ATLAS Tile Calorimeter”. In: *Nucl. Instrum. Meth. A* 615 (2010), pp. 158–  
 1533 181. doi: [10.1016/j.nima.2010.01.037](https://doi.org/10.1016/j.nima.2010.01.037).
- 1534 [30] ATLAS Collaboration. “Jet energy measurement and its systematic uncer-  
 1535 tainty in proton–proton collisions at  $\sqrt{s} = 7$  TeV with the ATLAS detec-  
 1536 tor”. In: *Eur. Phys. J. C* 75 (2015), p. 17. doi: [10.1140/epjc/s10052-014-3190-y](https://doi.org/10.1140/epjc/s10052-014-3190-y). arXiv: [1406.0076 \[hep-ex\]](https://arxiv.org/abs/1406.0076). PERF-2012-01.
- 1538 [31] Hung-Liang Lai, Marco Guzzi, Joey Huston, Zhao Li, Pavel M. Nadolsky,  
 1539 et al. “New parton distributions for collider physics”. In: *Phys. Rev. D* 82  
 1540 (2010), p. 074024. doi: [10.1103/PhysRevD.82.074024](https://doi.org/10.1103/PhysRevD.82.074024). arXiv: [1007.2241 \[hep-ph\]](https://arxiv.org/abs/1007.2241).
- 1542 [32] E. Abat et al. “Study of energy response and resolution of the ATLAS barrel  
 1543 calorimeter to hadrons of energies from 20 to 350 GeV”. In: *Nucl. Instrum.*  
 1544 *Meth. A* 621.1-3 (2010), pp. 134 – 150. doi: <http://dx.doi.org/10.1016/j.nima.2010.04.054>.
- 1546 [33] ATLAS Collaboration. “Jet energy measurement with the ATLAS detector  
 1547 in proton–proton collisions at  $\sqrt{s} = 7$  TeV”. In: *Eur. Phys. J. C* 73 (2013),  
 1548 p. 2304. doi: [10.1140/epjc/s10052-013-2304-2](https://doi.org/10.1140/epjc/s10052-013-2304-2). arXiv: [1112.6426 \[hep-ex\]](https://arxiv.org/abs/1112.6426). PERF-2011-03.
- 1550 [34] Nausheen R. Shah and Carlos E. M. Wagner. “Gravitons and dark matter in  
 1551 universal extra dimensions”. In: *Phys. Rev. D* 74 (2006), p. 104008. doi: [10.1103/PhysRevD.74.104008](https://doi.org/10.1103/PhysRevD.74.104008). arXiv: [hep-ph/0608140 \[hep-ph\]](https://arxiv.org/abs/hep-ph/0608140).
- 1553 [35] Jonathan L. Feng, Arvind Rajaraman, and Fumihiro Takayama. “Graviton  
 1554 cosmology in universal extra dimensions”. In: *Phys. Rev. D* 68 (2003), p. 085018.  
 1555 doi: [10.1103/PhysRevD.68.085018](https://doi.org/10.1103/PhysRevD.68.085018). arXiv: [hep-ph/0307375 \[hep-ph\]](https://arxiv.org/abs/hep-ph/0307375).
- 1557 [36] Paul H. Frampton and Pham Quang Hung. “Long-lived quarks?” In: *Phys.*  
 1558 *Rev. D* 58 (5 1998), p. 057704. doi: [10.1103/PhysRevD.58.057704](https://doi.org/10.1103/PhysRevD.58.057704).  
 1559 URL: <http://link.aps.org/doi/10.1103/PhysRevD.58.057704>.
- 1561 [37] C. Friberg, E. Norrbin, and T. Sjostrand. “QCD aspects of leptoquark pro-  
 1562 duction at HERA”. In: *Phys. Lett. B* 403 (1997), pp. 329–334. doi: [10.1016/S0370-2693\(97\)00543-1](https://doi.org/10.1016/S0370-2693(97)00543-1). arXiv: [hep-ph/9704214 \[hep-ph\]](https://arxiv.org/abs/hep-ph/9704214).
- 1564 [38] Herbert K. Dreiner. “An introduction to explicit R-parity violation”. In:  
 1565 (1997). arXiv: [hep-ph/9707435](https://arxiv.org/abs/hep-ph/9707435).

- 1566 [39] Edmond L. Berger and Zack Sullivan. “Lower limits on R-parity-violating  
 1567 couplings in supersymmetry”. In: *Phys. Rev. Lett.* 92 (2004), p. 201801. doi:  
 1568 [10.1103/PhysRevLett.92.201801](https://doi.org/10.1103/PhysRevLett.92.201801). arXiv: [hep-ph/0310001](https://arxiv.org/abs/hep-ph/0310001).
- 1569 [40] R. Barbieri, C. Berat, M. Besancon, M. Chemtob, A. Deandrea, et al. “R-  
 1570 parity violating supersymmetry”. In: *Phys. Rept.* 420 (2005), p. 1. doi: [10.1016/j.physrep.2005.08.006](https://doi.org/10.1016/j.physrep.2005.08.006). arXiv: [hep-ph/0406039](https://arxiv.org/abs/hep-ph/0406039).
- 1572 [41] M. Fairbairn et al. “Stable massive particles at colliders”. In: *Phys. Rept.* 438  
 1573 (2007), p. 1. doi: [10.1016/j.physrep.2006.10.002](https://doi.org/10.1016/j.physrep.2006.10.002). arXiv: [hep-ph/0611040](https://arxiv.org/abs/hep-ph/0611040).
- 1575 [42] Christopher F. Kolda. “Gauge-mediated supersymmetry breaking: Intro-  
 1576 duction, review and update”. In: *Nucl. Phys. Proc. Suppl.* 62 (1998), p. 266.  
 1577 doi: [10.1016/S0920-5632\(97\)00667-1](https://doi.org/10.1016/S0920-5632(97)00667-1). arXiv: [hep-ph/9707450](https://arxiv.org/abs/hep-ph/9707450).
- 1578 [43] Howard Baer, Kingman Cheung, and John F. Gunion. “A Heavy gluino as  
 1579 the lightest supersymmetric particle”. In: *Phys. Rev. D* 59 (1999), p. 075002.  
 1580 doi: [10.1103/PhysRevD.59.075002](https://doi.org/10.1103/PhysRevD.59.075002). arXiv: [hep-ph/9806361](https://arxiv.org/abs/hep-ph/9806361).
- 1581 [44] S. James Gates Jr. and Oleg Lebedev. “Searching for supersymmetry in  
 1582 hadrons”. In: *Phys. Lett. B* 477 (2000), p. 216. doi: [10.1016/S0370-2693\(00\)00172-6](https://doi.org/10.1016/S0370-2693(00)00172-6). arXiv: [hep-ph/9912362](https://arxiv.org/abs/hep-ph/9912362).
- 1584 [45] G. F. Giudice and A. Romanino. “Split supersymmetry”. In: *Nucl. Phys. B*  
 1585 699 (2004), p. 65. doi: [10.1016/j.nuclphysb.2004.11.048](https://doi.org/10.1016/j.nuclphysb.2004.11.048). arXiv:  
 1586 [hep-ph/0406088](https://arxiv.org/abs/hep-ph/0406088).
- 1587 [46] N. Arkani-Hamed, S. Dimopoulos, G. F. Giudice, and A. Romanino. “As-  
 1588 pects of split supersymmetry”. In: *Nucl. Phys. B* 709 (2005), p. 3. doi: [10.1016/j.nuclphysb.2004.12.026](https://doi.org/10.1016/j.nuclphysb.2004.12.026). arXiv: [hep-ph/0409232](https://arxiv.org/abs/hep-ph/0409232).
- 1590 [47] Glennys R. Farrar and Pierre Fayet. “Phenomenology of the Production,  
 1591 Decay, and Detection of New Hadronic States Associated with Supersym-  
 1592 metry”. In: *Phys. Lett.* B76 (1978), pp. 575–579. doi: [10.1016/0370-2693\(78\)90858-4](https://doi.org/10.1016/0370-2693(78)90858-4).
- 1594 [48] A. C. Kraan, J. B. Hansen, and P. Nevski. “Discovery potential of R-hadrons  
 1595 with the ATLAS detector”. In: *Eur. Phys. J.* C49 (2007), pp. 623–640. doi:  
 1596 [10.1140/epjc/s10052-006-0162-x](https://doi.org/10.1140/epjc/s10052-006-0162-x). arXiv: [hep-ex/0511014](https://arxiv.org/abs/hep-ex/0511014)  
 1597 [[hep-ex](#)].
- 1598 [49] K. A. Olive et al. “Review of Particle Physics”. In: *Chin. Phys.* C38 (2014),  
 1599 p. 090001. doi: [10.1088/1674-1137/38/9/090001](https://doi.org/10.1088/1674-1137/38/9/090001).
- 1600 [50] ATLAS Collaboration. “Search for massive, long-lived particles using mul-  
 1601 titrack displaced vertices or displaced lepton pairs in  $pp$  collisions at  $\sqrt{s} =$   
 1602 8 TeV with the ATLAS detector”. In: *Phys. Rev. D* 92 (2015), p. 072004.  
 1603 doi: [10.1103/PhysRevD.92.072004](https://doi.org/10.1103/PhysRevD.92.072004). arXiv: [1504.05162 \[hep-ex\]](https://arxiv.org/abs/1504.05162).  
 1604 SUSY-2014-02.

- 1605 [51] ATLAS Collaboration. “Search for charginos nearly mass degenerate with  
 1606 the lightest neutralino based on a disappearing-track signature in  $pp$  col-  
 1607 lisions at  $\sqrt{s} = 8$  TeV with the ATLAS detector”. In: *Phys. Rev. D* 88 (2013),  
 1608 p. 112006. doi: [10.1103/PhysRevD.88.112006](https://doi.org/10.1103/PhysRevD.88.112006). arXiv: [1310.3675](https://arxiv.org/abs/1310.3675)  
 1609 [[hep-ex](#)]. SUSY-2013-01.
- 1610 [52] ATLAS Collaboration. “Searches for heavy long-lived sleptons and R-Hadrons  
 1611 with the ATLAS detector in  $pp$  collisions at  $\sqrt{s} = 7$  TeV”. In: *Phys. Lett. B*  
 1612 720 (2013), p. 277. doi: [10.1016/j.physletb.2013.02.015](https://doi.org/10.1016/j.physletb.2013.02.015). arXiv:  
 1613 [1211.1597](https://arxiv.org/abs/1211.1597) [[hep-ex](#)]. SUSY-2012-01.
- 1614 [53] ATLAS Collaboration. “Searches for heavy long-lived charged particles  
 1615 with the ATLAS detector in proton–proton collisions at  $\sqrt{s} = 8$  TeV”. In: *JHEP* 01 (2015), p. 068. doi: [10.1007/JHEP01\(2015\)068](https://doi.org/10.1007/JHEP01(2015)068). arXiv:  
 1616 [1411.6795](https://arxiv.org/abs/1411.6795) [[hep-ex](#)]. SUSY-2013-22.
- 1617 [54] ATLAS Collaboration. “Search for metastable heavy charged particles with  
 1618 large ionisation energy loss in  $pp$  collisions at  $\sqrt{s} = 8$  TeV using the AT-  
 1619 LAS experiment”. In: *Eur. Phys. J. C* 75 (2015), p. 407. doi: [10.1140/epjc/s10052-015-3609-0](https://doi.org/10.1140/epjc/s10052-015-3609-0). arXiv: [1506.05332](https://arxiv.org/abs/1506.05332) [[hep-ex](#)]. SUSY-  
 1620 2014-09.
- 1621 [55] ATLAS Collaboration. “Search for heavy long-lived charged  $R$ -hadrons  
 1622 with the ATLAS detector in  $3.2 \text{ fb}^{-1}$  of proton–proton collision data at  
 1623  $\sqrt{s} = 13$  TeV”. In: *Phys. Lett. B* 760 (2016), pp. 647–665. doi: [10.1016/j.physletb.2016.07.042](https://doi.org/10.1016/j.physletb.2016.07.042). arXiv: [1606.05129](https://arxiv.org/abs/1606.05129) [[hep-ex](#)].
- 1624 [56] “dE/dx measurement in the ATLAS Pixel Detector and its use for particle  
 1625 identification”. In: (2011).
- 1626 [57] ATLAS Collaboration. “The ATLAS Simulation Infrastructure”. In: *Eur.  
 1627 Phys. J.* C70 (2010), pp. 823–874. doi: [10.1140/epjc/s10052-010-1429-9](https://doi.org/10.1140/epjc/s10052-010-1429-9). arXiv: [1005.4568](https://arxiv.org/abs/1005.4568) [[physics.ins-det](#)].



1632 DECLARATION

---

1633 Put your declaration here.

1634 *Berkeley, CA, September 2016*

1635

---

Bradley Axen



1636

1637 COLOPHON

1638

Not sure that this is necessary.